



HAL
open science

Interplay between melt infiltration and deformation in the deep lithospheric mantle (External Liguride ophiolite, North Italy)

Károly Hidas, Giulio Borghini, Andrea Tommasi, Alberto Zanetti, Elisabetta Rampone

► To cite this version:

Károly Hidas, Giulio Borghini, Andrea Tommasi, Alberto Zanetti, Elisabetta Rampone. Interplay between melt infiltration and deformation in the deep lithospheric mantle (External Liguride ophiolite, North Italy). *Lithos*, 2020, 10.1016/j.lithos.2020.105855 . hal-03016316

HAL Id: hal-03016316

<https://hal.umontpellier.fr/hal-03016316>

Submitted on 20 Nov 2020

HAL is a multi-disciplinary open access archive for the deposit and dissemination of scientific research documents, whether they are published or not. The documents may come from teaching and research institutions in France or abroad, or from public or private research centers.

L'archive ouverte pluridisciplinaire **HAL**, est destinée au dépôt et à la diffusion de documents scientifiques de niveau recherche, publiés ou non, émanant des établissements d'enseignement et de recherche français ou étrangers, des laboratoires publics ou privés.

Author copy of the final (peer-reviewed) version

Article published in *Lithos* in November 2020

Please, reference to: Hidas, K., Borghini, G., Tommasi, A., Zannetti, A., Rampone, E. (2020) Interplay between melt infiltration and deformation in the deep lithospheric mantle (External Liguride ophiolite, North Italy). *Lithos*, doi : 10.1016/j.lithos.2020.105855.

Interplay between melt infiltration and deformation in the deep lithospheric mantle (External Liguride ophiolite, North Italy)

Károly Hidas^{a,b,*}, Giulio Borghini^c, Andréa Tommasi^d, Alberto Zanetti^e, Elisabetta Rampone^f

^a Instituto Andaluz de Ciencias de la Tierra (IACT), CSIC & Universidad de Granada, Avenida de las Palmeras 4, 18100, Armilla, Granada, Spain

^b Departamento de Investigación y Prospectiva Geocientífica, Instituto Geológico y Minero de España, Calle de la Calera 1, 28760, Tres Cantos, Madrid, Spain

^c Dipartimento di Scienze della Terra, Università degli Studi di Milano, via Botticelli 23, 20133 Milano, Italy

^d Géosciences Montpellier, CNRS & Université de Montpellier, Place E. Bataillon, 34095, cedex 5, Montpellier, France

^e Istituto di Geoscienze e Georisorse (IGG), CNR, S.S. of Pavia, via Ferrata 1, I-27100 Pavia, Italy

^f Dipartimento di Scienze della Terra dell'Ambiente e della Vita (DISTAV), Università di Genova, 16132 Genova, Italy

A B S T R A C T

Mantle peridotites from the External Liguride Jurassic ophiolites (Northern Apennines, Italy) show diffuse occurrence of pyroxenite bands, recording melt migration and crystallization at the lithosphere-asthenosphere boundary, during old, pre-Jurassic stages of their subcontinental lithospheric mantle evolution. We present coupled microstructural and geochemical study of profiles across various types of pyroxenite-peridotite layering in these ophiolites, aiming to constrain the relative timing and potential interplay between melt infiltration and mantle deformation. The mantle sequence is composed of lherzolite and harzburgite, occasionally interleaved with dunite, crosscut by centimeter- to decimeter-wide pyroxenite layers. The peridotites have a porphyroclastic texture and show a penetrative tectonic foliation subparallel to the pyroxenite layering. Peridotite-pyroxenite contacts are irregular at the grain scale. Olivine and pyroxenes in both peridotites and pyroxenites record moderate to strong crystallographic preferred orientations (CPO) with alignment of olivine [100] and pyroxenes [001] axes subparallel to the stretching lineation marked by olivine and pyroxenes elongation. This is compatible with coeval deformation of olivine and pyroxenes during a high-temperature, spinel lherzolite-facies deformation event. The major and trace element compositions of peridotites record a metasomatic imprint that decreases with distance from the pyroxenite layers, whereas the strength of the olivine CPO decreases from the country peridotites towards the pyroxenite layers. The parallelism between pyroxenite layers and the peridotite foliation, their irregular contacts, as well as the spatial correlation between CPO and geochemical changes, are consistent with *syn-* to late-kinematic emplacement of the pyroxenites. These observations point to a strong interplay between deformation and melt transport processes in the mantle, characterized by melt focusing in conduits parallel to the foliation and changes in the mantle deformation processes due to the presence of melts. Exhumation of this mantle section in the Jurassic resulted in partial replacement of the spinel-facies assemblage by a plagioclase-bearing assemblage. Topotaxial relationship between plagioclase and precursor spinel-facies minerals suggests that this exhumation was not associated with pervasive deformation of the peridotite, but rather accommodated by deformation localized in discrete shear zones, not sampled in the present study.

Keywords:

Pyroxenite

EBSD

Mantle deformation

Melt-rock reaction

Peridotite

Microstructures

1. Introduction

Deep melt infiltration and melt-peridotite interaction are considered among the most efficient processes in creating small-scale heterogeneity in the upper mantle (e.g., Borghini et al., 2013; Donnelly et al., 2004; Lambart et al., 2012; Mallik and Dasgupta, 2012; Tommasi and Vauchez, 2015; Varas-Reus et al., 2018). These processes control mineralogical

changes in mantle rocks towards both pyroxene-rich and/or refractory (i.e., harzburgitic-dunitic) peridotite lithologies. Pyroxenites represent diffuse compositional and rheological heterogeneities in the deep lithosphere (e.g., Bodinier and Godard, 2014; Frets et al., 2012; Henry et al., 2017; Hidas et al., 2013) and, although volumetrically subordinated to peridotites, they play a key role in mantle melting processes (e.g., Brunelli et al., 2018; Hirschmann and Stolper, 1996; Kogiso et al., 2004; Lambart et al., 2013; Lambart et al., 2016; Marchesi et al., 2013; Phipps Morgan, 2001; Shorttle and Maclennan, 2011). For instance, pyroxenite-bearing veined mantle is often invoked as the source of oceanic basalts (e.g., Lambart et al., 2016 and references therein). Mantle

* Corresponding author at: Instituto Geológico y Minero de España, Calle de la Calera 1, 28760, Tres Cantos, Madrid, Spain.

E-mail address: k.hidas@igme.es (K. Hidas).

domains affected by infiltration of pyroxenite-derived melts also represent potential proxies of Enriched-MORB mantle sources (Borghini et al., 2013; Borghini et al., 2020; Salters and Dick, 2002). In addition, such fertile components can influence magma transport through peridotites by nucleating magmatic channels that potentially control the melt extraction dynamics from the mantle (e.g., Katz and Weatherley, 2012).

Large exposures of pyroxenite-bearing veined mantle have been documented in orogenic and ophiolitic ultramafic massifs (e.g., Bodinier and Godard, 2014). Studies on these pyroxenite-peridotite associations have evidenced the important role of melt-peridotite reactions in the origin of deep-seated magmatic pyroxenites, suggesting that pyroxenites could not represent simple magmatic intrusions, rather they result from melt infiltration and in situ melt-peridotite interactions (e.g., Borghini et al., 2016; Garrido and Bodinier, 1999; Le Roux, 2008; Tilhac et al., 2016; Tilhac et al., 2017; Tilhac et al., 2020; Varas-Reus et al., 2016). However, some critical aspects of the origin of pyroxenites at deep mantle levels are still poorly constrained. One of the main unresolved issues concerns the mechanisms governing the formation of pyroxenite layering in the deep lithospheric mantle. Opening of veins by brittle fracturing under these conditions ($P > 1.5$ GPa, $T > 1000$ °C) is only possible in presence of very high pore fluid pressure (e.g., Kelemen et al., 1995b; Kelemen et al., 1997). Moreover, depending on melt composition and P-T conditions, evolved pyroxenite- or eclogite-derived melts often react with peridotite promoting crystallization and melt consumption that would drastically decrease the peridotite porosity inhibiting further melt transport (e.g., Lambart et al., 2012; Rosenthal et al., 2014). In fact, recent microstructural studies on pyroxenite-peridotite assemblages have revealed that pyroxenite emplacement in the upper mantle is often related to synkinematic melt percolation (Frets et al., 2012; Frets et al., 2014; Henry et al., 2017; Kaczmarek et al., 2015; Le Roux et al., 2008; Soustelle et al., 2009; Tommasi et al., 2016), highlighting strong positive feedbacks between melt transport and ductile deformation in the deep lithospheric mantle.

Mantle peridotites from the External Liguride ophiolites (Northern Apennines, Italy) represent sectors of subcontinental lithospheric mantle that were tectonically exhumed during Jurassic rifting and opening of the Alpine Tethys ocean. They show diffuse occurrence of pyroxenite bands, recording melt migration and intrusion processes that occurred at deep lithospheric conditions during old, pre-Jurassic stages of their subcontinental mantle history (e.g., Borghini et al., 2013; Borghini et al., 2016; Borghini et al., 2020; Montanini et al., 2006; Montanini et al., 2012; Montanini and Tribuzio, 2015; Rampone et al., 2020). Unlike other ophiolitic peridotites from the Alpine realm, the EL pyroxenite-peridotite mantle sequences escaped the melt-rock interaction processes related to Jurassic emplacement on the ocean floor in an ocean-continent transition environment (e.g., Picazo et al., 2016; Piccardo et al., 2004; Rampone et al., 2004; Rampone et al., 2008; Rampone et al., 2020). The lack of overprint by such younger and shallower events resulted in the preservation of the chemical and isotopic variability acquired during the melt infiltration and pyroxenitic melt-rock reaction at deep mantle levels (Borghini et al., 2013, 2016, 2020).

Despite the careful geochemical characterization of the External Liguride mantle sequences in the past decades, the timing of deformation resulting in the tectonic foliation of the host peridotites relative to the formation of dunite-harzburgite layers and pyroxenites has not been constrained yet. In this paper, we present a detailed microstructural and geochemical study of a series of profiles across various types of pyroxenite-peridotite layering, which sheds light on the potential interplay between melt infiltration and pyroxenite emplacement, responsible of local chemical modification of the host peridotite, and mantle deformation in the deep lithosphere.

2. Geological setting and field exposure of mantle rocks

The Alpine-Apennine ophiolites are remnants of the oceanic lithosphere of the Alpine Tethys, a rather narrow oceanic basin developed by divergence of Europa and Adria blocks during the pre-Jurassic rifting and Middle Jurassic opening of the Northern Atlantic (Bill et al., 2001; Lemoine and Trümpy, 1987; Rampone et al., 2020). They are predominantly composed of mantle peridotites (exhumed at the sea floor) and largely subordinate crustal rocks (gabbroic intrusions and discontinuous basaltic cover). Accordingly, they were defined as “passive margin ophiolites”, and are considered as fossil analogues of present-day passive continental margins, such as the Iberian margin, and/or slow- to ultra-slow-spreading ridges, such as the Gakkel and Southwest Indian ridges (Manatschal and Müntener, 2009; Marroni and Pandolfi, 2007; Müntener et al., 2004; Müntener and Piccardo, 2003; Rampone et al., 2000; Rampone et al., 2020; Sanfilippo and Tribuzio, 2011; Tribuzio et al., 2016).

Most Alpine-Apennine mantle bodies record widespread evidence for thermomechanical erosion and refertilization processes related to asthenospheric upwelling during rifting and oceanization of the subcontinental lithosphere related to the opening of the Jurassic Tethys (Müntener et al., 2004; Rampone et al., 1997; Rampone et al., 2004; Rampone et al., 2008; Rampone et al., 2020). A notable exception is the External Liguride (hereafter EL) unit (Fig. 1a–b), which has not been overprinted by shallow lithospheric melt-rock interaction processes and preserves the geochemical signature of the pre-rifting subcontinental lithospheric mantle (Borghini et al., 2011; Montanini and Harlov, 2006; Rampone et al., 1995).

The EL ophiolites consist of several mantle peridotite bodies (up to kilometer scale), with minor MOR-type basalts and rare gabbroic rocks, occurring as large olistoliths within Cretaceous sedimentary mélanges obducted during the closure of the oceanic basin (Montanini et al., 2008; Rampone et al., 1993; Rampone et al., 1995; Tribuzio et al., 2004). Few mantle outcrops in the northern sector of EL ophiolites preserved rare garnet-bearing pyroxenites recording an early stage of equilibration at ca. 2.8 GPa and 1100 °C (Montanini et al., 2006; Montanini et al., 2012). These pyroxenites are considered to crystallize from melts produced by partial melting of recycled crustal eclogites (Montanini and Tribuzio, 2015).

Peridotite-pyroxenite associations investigated in this study are from three, hundred-meter wide peridotite slivers from the eastern sector of External Liguride unit (Borghini et al., 2013, 2016; Rampone et al., 1995) (Fig. 1b). These ultramafic bodies consist of moderately serpentinized peridotites crosscut by pyroxenite layers preserving mantle textures and assemblages. Peridotites are mostly Iherzolites (>80% of the exposed outcrops) but modal variability towards harzburgite (<10% of the exposed outcrops) and dunite lithologies (<10% of the exposed outcrops) is also observed locally in centimeter-scale refractory peridotite layers. Dunite layers are typically hosted in Iherzolite or harzburgite along sharp yet, at the grain-scale, irregular lithological boundaries. Pyroxenites occur within peridotites as cm-scale layers (from <1 cm to 12–15 cm) subparallel to the tectonite foliation plane of the host peridotites. Pyroxenite-peridotite contacts are sharp, but irregular (Fig. 1c). They mostly consist of spinel websterites and clinopyroxenites. Pyroxenite abundance and distribution are variable across the massif, and they locally occur as layers parallel to the lithological variations (harzburgite and/or dunite layers) of the host peridotite. In some decimeters-sized outcrops, pyroxenite-peridotite proportion is 1:1, showing pyroxenite layers spaced a few centimeters apart (Supplementary Fig. S1c) (Borghini et al., 2013, 2016).

3. Petrological background

Previous works on peridotites from the study area have documented a rather fertile chemical signature coupled to extremely depleted Sr and Nd isotopic composition, suggesting that the peridotites were

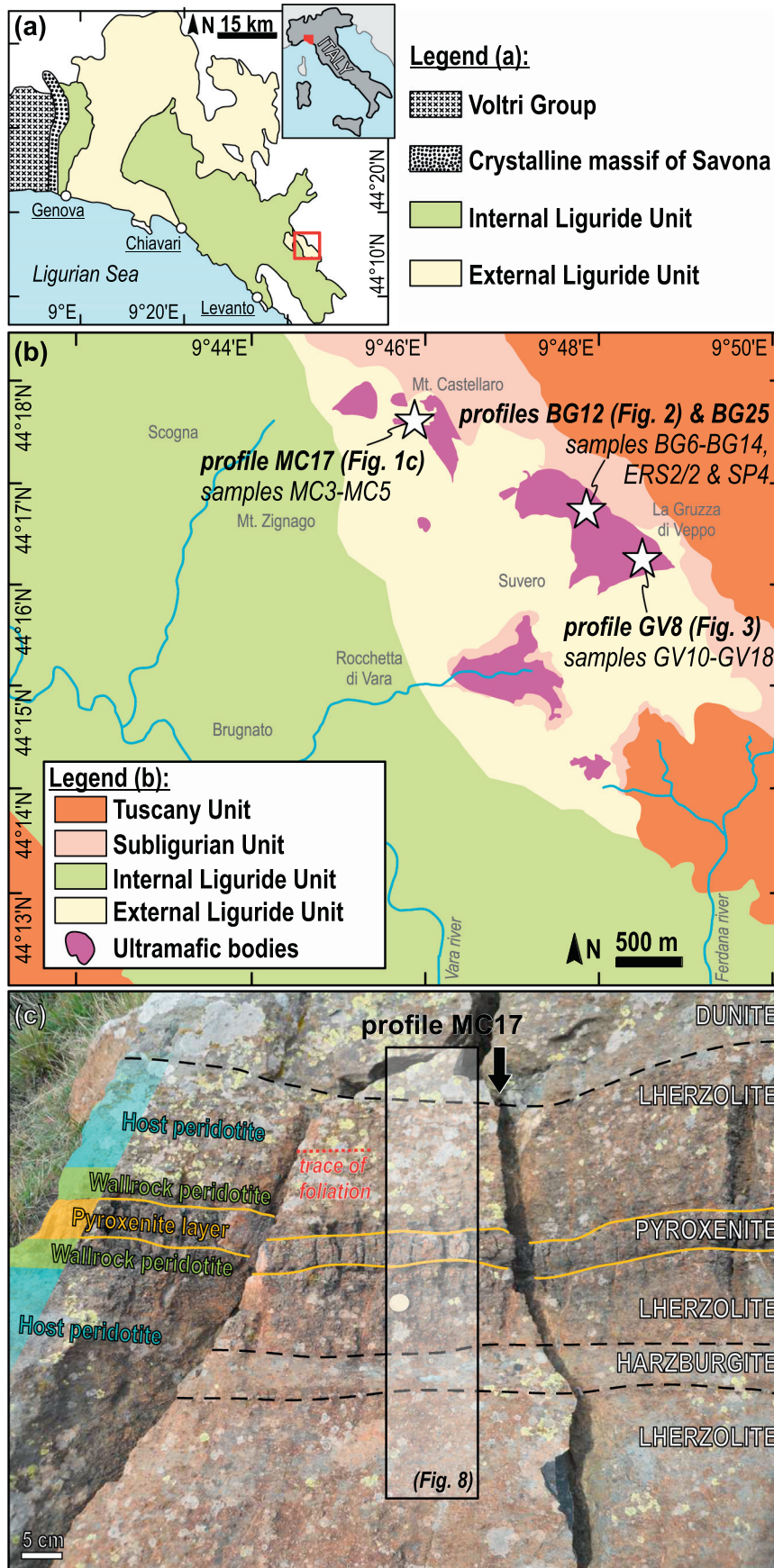


Fig. 1. Schematic maps of main tectonic units of the Northern Apennines (a) and the sampling sites in the ultramafic bodies of the External Liguride Unit (b). Compilation after Borghini et al., 2016 and references therein. For the documentation of profile BG25 and other samples without citation to figures in (b), see Supplementary Figs. S1-S2. (c) Field exposure of a representative pyroxenite-peridotite sequence (profile MC17).

MORB-type fertile asthenospheric mantle accreted to the base of the lithosphere since the Proterozoic (Rampone et al., 1995). On the basis of bulk-rock and mineral chemistry features, the pyroxenites in the EL-ophiolite were interpreted as secondary-type pyroxenites originated from segregation of a tholeiitic low-MgO melt [$X_{\text{Mg}} = \text{Mg}/(\text{Mg} + \text{Fe}_{\text{tot}}) = 0.44\text{--}0.56$], which reacted to some extent with the host peridotite during mantle infiltration (Borghini et al., 2016, 2020). The REE signature of bulk rocks and clinopyroxenes indicates that most pyroxenites originally formed as garnet-bearing assemblages, yet garnet was completely replaced by later spinel-facies subsolidus recrystallization (Borghini et al., 2016). The inferred occurrence of garnet among the primary mineral association indicates crystallization at relatively high pressure (>1.5 GPa, Borghini and Fumagalli, 2018; Borghini et al., 2016).

Pyroxenites and associated peridotites preserve centimeter-scale chemical and isotopic gradients, which were revealed by chemical and Sr—Nd isotope profiles (on bulk-rocks and minerals) perpendicular to the lithological contact (Borghini et al., 2013). The interaction between pyroxenite-derived melts and the adjacent peridotite wall rock produced trace element and Nd-isotope enriched mantle domains by (Borghini et al., 2020). The longest geochemical profile revealed that the REE perturbation in clinopyroxene persists in the host peridotite ca. 20 cm from the contact with the pyroxenite. Geochemical modelling indicates that such REE variations were produced by reactive percolation of melts coming from pyroxenite veins, resulting in olivine assimilation and pyroxene crystallization (see Borghini et al., 2020 for more details).

Local Sm—Nd isochrons, defined by pyroxenite and adjacent peridotite, yielded Paleozoic ages for pyroxenite emplacement and metasomatism of the host peridotites (424–452 Ma, Late Ordovician–Silurian ages; Borghini et al., 2013, 2016). This event significantly predated the Jurassic exhumation of the EL mantle segments on the ocean floor (Borghini et al., 2016; Rampone et al., 2020). During this latter stage, both peridotites and pyroxenites were partially recrystallized at subsolidus plagioclase-facies conditions (870–930 °C; Basch et al., 2020; Borghini et al., 2011; Borghini et al., 2016). Thermobarometric estimates on the peridotites provided a relatively cold decompressional evolution from 0.70 to 0.43 GPa at 800–900 °C (Fumagalli et al., 2017). Internal Sm—Nd isochrones dated the plagioclase-facies recrystallization at 178 ± 8 Ma, consistent with the Mesozoic continental rifting that led to the opening of the Jurassic Tethys (Borghini et al., 2016). This rather cold decompressional evolution allowed these mantle domains to preserve the ancient chemical and isotopic variability acquired during melt infiltration, melt-rock reaction, and pyroxenite segregation at deep mantle levels (Borghini et al., 2013, 2016, 2020).

4. Sampling and analytical methods

4.1. Sampling and sample preparation

The EL peridotites are variously serpentinized, while pyroxenites are typically fresh. We performed combined microstructural and chemical investigations on profiles normal to the peridotite-pyroxenite layering including i) a pyroxenite layer (up to 12 cm wide), ii) the wall-rock peridotite (up to 4 cm from the pyroxenite boundary), iii) the host peridotite (between 4 cm and 20 cm from the pyroxenite boundary), and iv) the “country” peridotite, (sampled in pyroxenite-free outcrops >2 m away from any pyroxenite layer) (Table 1, Figs. 1–3, Supplementary Fig. S1; see also Borghini et al., 2013, 2020). Data presented in this paper are from two ultramafic bodies and refer to: i) three pyroxenite-peridotite cross sections including pyroxenite, wall-rock and host peridotites (profiles BG25, Supplementary Fig. S1c–d; GV8, Fig. 3; and MC17, Fig. 1c), ii) one pyroxenite-free, dunite-lherzolite profile representative of the country peridotite (profile BG12, Fig. 2), and iii) several individual pyroxenite and peridotite

samples complementary to the profiles (see Fig. 1b and Table 1 for location and sample summary).

Country peridotites (except for BG12), pyroxenites (GV10, BG13, MC5), and the 23 cm-long profile GV8 were previously investigated by Borghini et al. (2013, 2016, 2020) for their major and trace element compositions. The three new profiles (BG12, BG25 and MC17) documented in this study include the mineralogical variability observed in peridotite, not yet investigated in previous works. The 7 cm-long pyroxenite-free profile BG12 samples a centimeter-wide dunite layer within the country peridotite, far from any pyroxenite layer (Fig. 2, Supplementary Fig. S1a–b). The 16 cm-long profile BG25 is characterized by few-centimeter wide layers of dunite, lherzolite, dunite, pyroxenite, lherzolite, dunite, lherzolite (Supplementary Fig. S1c–d). The 40 cm-long profile MC17 is sampled perpendicularly to a layered association composed by dunite, lherzolite, pyroxenite (about 8 cm wide), lherzolite, harzburgite and clinopyroxene-poor lherzolite (Fig. 1c; Supplementary Fig. S1e–f).

Thin sections were cut perpendicular to the foliation and parallel to the stretching lineation of the host peridotite (i.e., XZ structural section), wherever this latter was observed (samples marked with a star in Table 1). In the pyroxenite samples, the thin section plane has the same geographic orientation as that in the closest peridotite tectonite. Where stretching lineation could not be defined in the peridotite, the thin sections were cut in a random plane perpendicular to the foliation, but the orientation was kept constant for all samples in the corresponding cross section, wherever it was possible. Standard petrographic thin sections were ground to a thickness of approximately 100 μm and were polished using diamond paste with 3- and 1- μm grain sizes. Final surface of the thin sections was achieved after 45 min chemical and mechanical polishing using Buehler MasterMet colloidal silica polishing suspension.

4.2. Microstructural and chemical analyses

The uncoated thin sections were mounted with conductive carbon tape to reduce charging. Analyses were carried out at high vacuum (in the range of 10^{-5} mbar) using a (1) Zeiss EVO MA 15 SEM equipped with Oxford Instruments Nordlys Nano electron backscatter diffraction (EBSD) system at the Instituto Andaluz de Ciencias de la Tierra (Granada, Spain) and (2) JEOL JSM 5600 SEM equipped with Oxford Instruments Nordlys II EBSD system at Géosciences Montpellier (Montpellier, France). In both cases, EBSD patterns were indexed by the AZtec data acquisition software, and instrumental settings were 24–25 mm working distance, 17–20 kV acceleration voltage using a tungsten filament as a source of electrons and camera settings of 4×4 binning and low (0) gain. EBSD maps cover at least 80% of the thin section surface with grid steps of 17–45 μm , depending on the grain size. All major constituent minerals of the rocks were included in the phase list. The percentage of indexed points in the raw maps ranges from ca. 30 to 80% due to variable alteration state of the rocks, which typically affects olivine and plagioclase. EBSD data with indexing rates of the raw maps inferior to 60% are used only for plotting the crystallographic orientation of the minerals, and the calculated quantitative microstructural parameters have been omitted in the manuscript (e.g., Fig. 4 and Table 1). The original unfiltered dataset can be found in Supplementary Table S1.

Post-acquisition data treatment to clean raw maps by filling non-indexed pixels based on neighboring pixel orientation up to maximum five identical neighbors, as well as removing wild-spikes were carried out using the built-in functions of the Oxford/HKL Channel 5 software package. Grain boundaries are defined at 12° minimum misorientation between neighboring pixels of the same phase (segmentation angle). Grain segmentation was accomplished using the ‘calcGrains’ built-in function of MTEX v.4.5.2 Matlab toolbox (<https://mtextoolbox.github.io/>; Bachmann et al., 2010; Bachmann et al., 2011; Hielscher and Schaefer, 2008). For the visualization of neighboring grain crystal orientations, we used the ‘crystalShape’ built-in function of MTEX v.5.2.7.

COUNTRY PERIDOTITE
PROFILE BG12

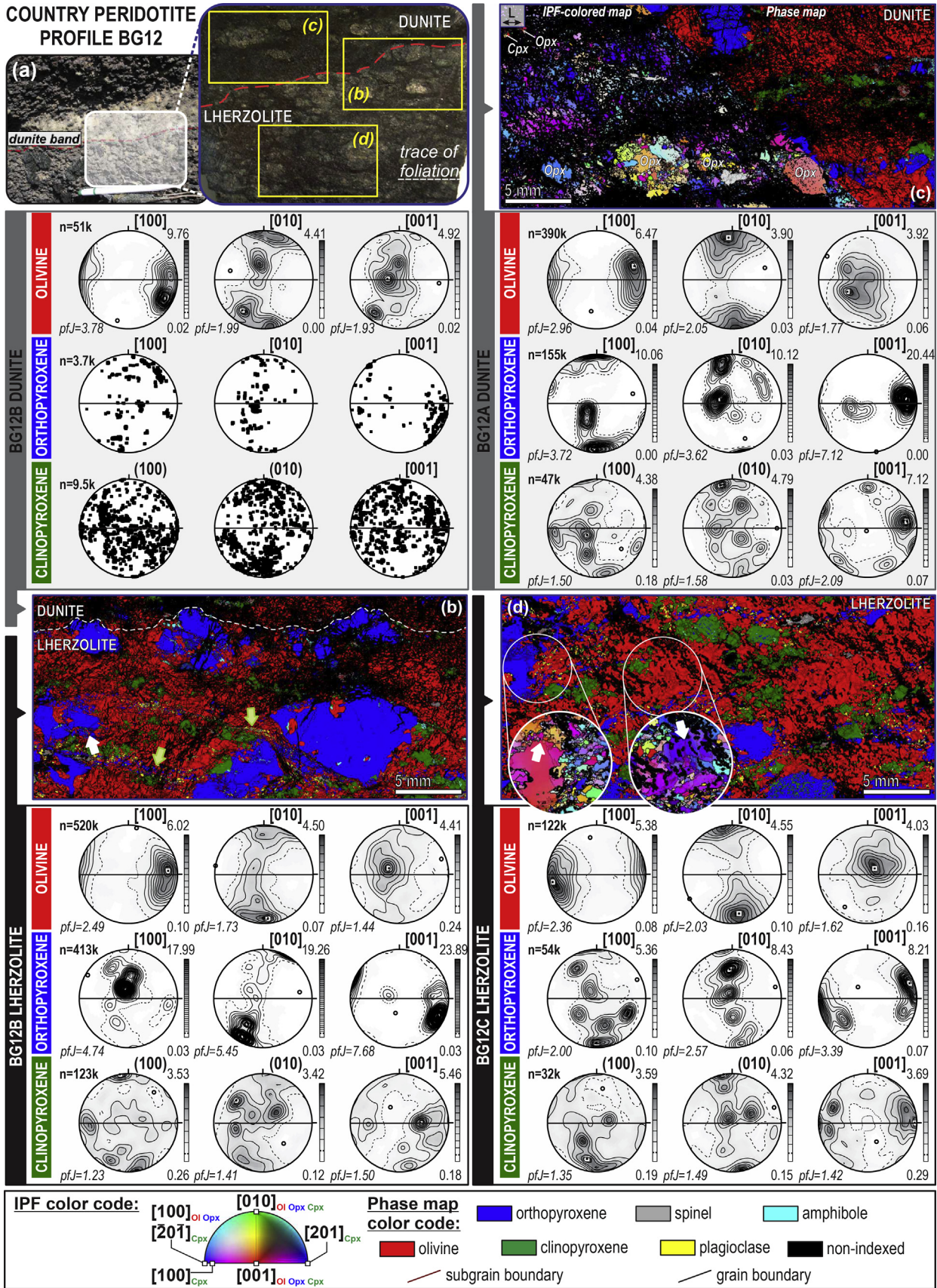


Fig. 2. (a) Field exposure of the pyroxenite-free, compositionally heterogeneous country peridotite profile BG12, and the location of thin sections shown in (b-d). (b-d) Microstructure and CPO of the main constituent phases in the dunite and in the lherzolite. The left-hand side of (c) and insets in (d) are color-coded with respect to the lineation in the crystal reference frame (inverse pole figure; IPF). The lineation direction is shown in the top-left corner of (c), indicated with L and an arrow. In the IPF-colored maps, spinel, plagioclase and amphibole are not considered and displayed in gray color. White arrows in (b) and in the insets of (d) indicate evidence for recrystallization in orthopyroxene at the porphyroclast edges and around olivine-filled bulges, and subgrain boundaries perpendicular to the elongation direction in olivine. Green arrows in (b) highlight fine-grained, anastomosing pyroxene-rich domains that are distributed subparallel to the foliation plane. See text for further details. Note that images in the figure are cropped out from raw EBSD maps; see Supplementary Fig. S2 for the entire maps. Pole figures are lower-hemisphere, equal-area stereographic plots using all pixels obtained in the maps with contours at 0.5 multiples of a uniform distribution; n: number of pixels, pfJ (in italic): scalar measure of the strength of the axis orientation in the pole figure. Contouring is omitted in samples with low number of grains (<10 k pixels; see Supplementary Table S1 for dataset). The samples were cut oriented and horizontal line denotes the foliation; lineation is at 90°. (For interpretation of the references to color in this figure legend, the reader is referred to the web version of this article.)

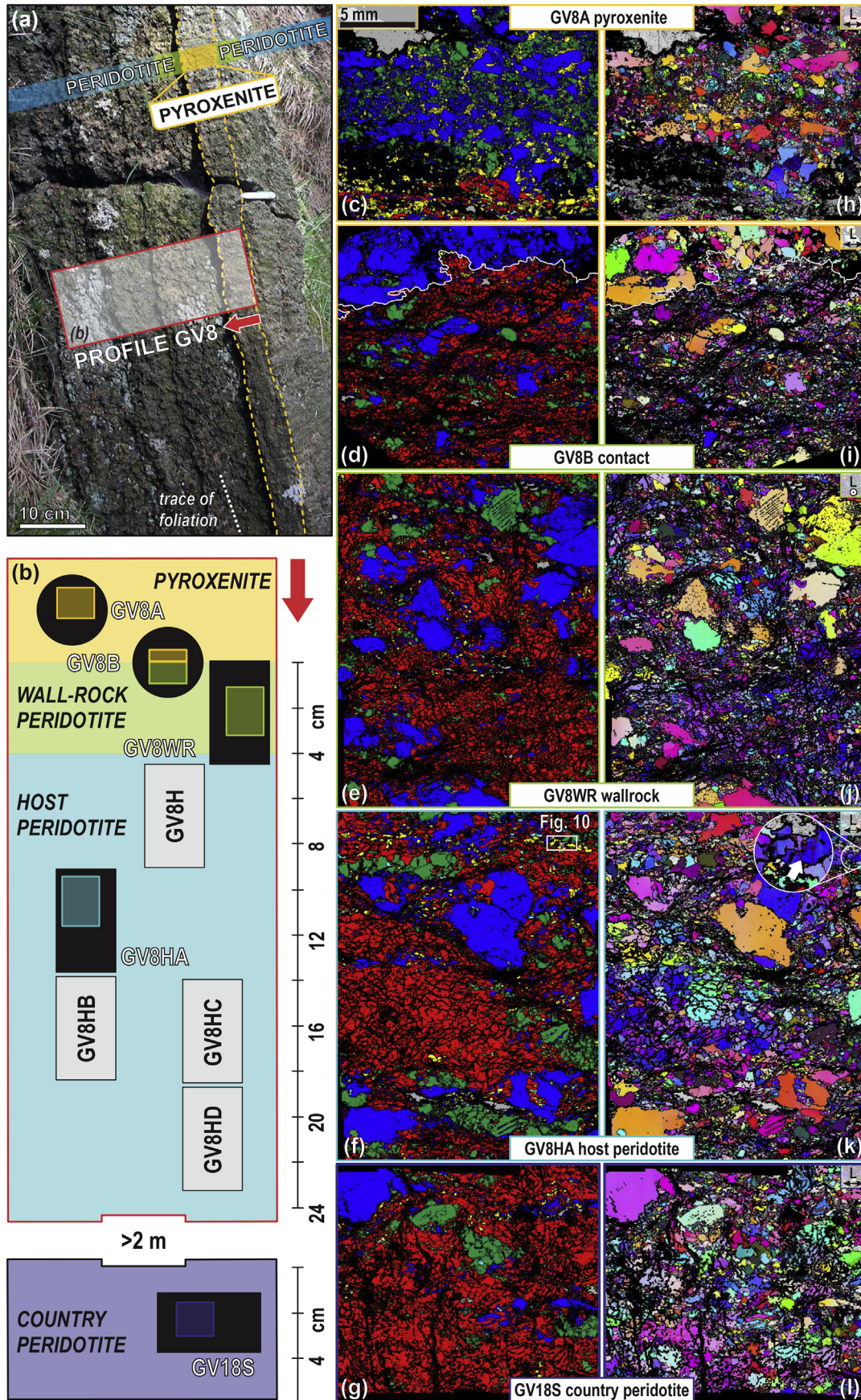


Fig. 3. Field exposure (a), thin section location (b), microstructure (c-g) and CPO of olivine, orthopyroxene and clinopyroxene (h-l) in the pyroxenite-peridotite profile GV8. In (h-l) the maps are color-coded with respect to the lineation in the crystal reference frame (inverse pole figure; IPF). The lineation direction is shown in the top-right corner of each map, indicated with L and an arrow (in case of sample GV8WR it is out of plane). In (b), areas in light gray (i.e., samples not shown in the figure) and black (i.e., samples shown in the figure) indicate position and orientation of thin sections, while colored boxes correspond to EBSD maps presented in (c-l). Note that images in (c-l) are cropped out from raw EBSD maps; see Supplementary Fig. S2 for the entire maps. White square in (f) indicates the location of the mineral assemblage shown in Fig. 10 (note that images and underlying data are rotated by 90° between the figures). Inset in (k) shows subgrain boundaries perpendicular to the elongation direction of olivine. Color-coding of the EBSD maps is the same as in Fig. 2.

Table 1

Field exposure, modal composition and main microstructural characteristics of the studied EL mantle rocks. The samples are grouped by their provenance from top to bottom as country peridotites, profiles BG12, BG25, MC17 and GV8, as well as other pyroxenite-peridotite assemblages. See Fig. 1 for location, text for sampling strategy and Supplementary Table S1 for the full microstructural dataset.

| Sample no. | Lithology (Type) | Exposure | | | Modal composition [area %] | | | | | | Quantitative texture parameters | | | |
|------------|----------------------|------------------------------|--------|---------|----------------------------|-----|-----|-----|-----|------|---------------------------------|-------|--------|--------|
| | | Latitude (N) / Longitude (E) | t | d | Ol | Opx | Cpx | Spl | Amp | Pl | BA(Ol) | M(Ol) | M(Opx) | M(Cpx) |
| BG6 | LHZ (C) | 44°16'45.03" / 9°47'38.94" | >2 m | >2 m | 70 | 18 | 10 | 1 | 0.1 | 1.4 | 0.71 | 0.19 | 0.15 | 0.06 |
| GV18 | LHZ (C) | 44°16'15.86" / 9°48'27.96" | >2 m | >2 m | 54 | 29 | 13 | 1 | 0.5 | 2.6 | 0.72 | 0.18 | 0.24 | 0.09 |
| ERS2/2* | LHZ (C) | 44°16'48.56" / 9°47'42.88" | >2 m | >2 m | 55 | 34 | 7 | 2 | 0.1 | 2.1 | 0.85 | 0.12 | na | 0.04 |
| ERS2/2B* | LHZ (C) | 44°16'48.56" / 9°47'42.88" | >2 m | >2 m | 66 | 16 | 15 | 2 | 0.2 | 2.0 | 0.95 | 0.15 | 0.19 | 0.07 |
| SP4* | LHZ (C) | 44°16'46.35" / 9°47'46.12" | >2 m | >2 m | 68 | 8 | 21 | 1 | 0.6 | 1.9 | 0.78 | 0.13 | 0.14 | 0.05 |
| BG12A* | DUN (C) | 44°16'46.22" / 9°47'46.63" | <7 cm | <2 cm | 63 | 25 | 8 | 2 | 2.2 | 0.0 | 0.70 | 0.25 | 0.23 | 0.07 |
| BG12B* | DUN-LHZ (C) | 44°16'46.22" / 9°47'46.63" | <5 cm | contact | 48 | 35 | 11 | 2 | 1.0 | 2.1 | 0.81 | 0.17 | 0.32 | 0.04 |
| BG12C* | LHZ (C) | 44°16'46.22" / 9°47'46.63" | >2 m | >2 cm | 57 | 25 | 15 | 1 | 0.2 | 1.9 | 0.69 | 0.20 | 0.19 | 0.04 |
| BG25A | DUN-LHZ (H) | 44°16'49.16" / 9°47'43.37" | <5 cm | 9.2 cm | 55 | 21 | 18 | 3 | 0.5 | 2.0 | 0.70 | 0.14 | 0.13 | 0.04 |
| BG25B | LHZ-HZB (W) | 44°16'49.16" / 9°47'43.37" | <5 cm | 3 cm | 46 | 26 | 24 | 2 | 0.6 | 0.9 | 0.64 | 0.17 | 0.21 | 0.04 |
| BG25C | LHZ (X) | 44°16'49.16" / 9°47'43.37" | <2 cm | 1 cm | 46 | 29 | 22 | 1 | 0.2 | 1.9 | 0.76 | 0.10 | na | 0.02 |
| | PYX (X) | | <3 cm | - | 1 | 34 | 57 | 7 | 0.5 | 0.5 | na | na | na | 0.11 |
| BG25D | HZB (W) | 44°16'49.16" / 9°47'43.37" | <3 cm | 3.7 cm | 44 | 38 | 15 | 2 | 0.1 | 0.7 | 0.69 | 0.17 | 0.18 | 0.02 |
| MC17A1* | DUN-LHZ (H) | 44°17'42.58" / 9°45'44.36" | <7 cm | 19.4 cm | 30 | 40 | 25 | 2 | 0.5 | 2.3 | 0.84 | 0.13 | na | 0.04 |
| MC17A2* | LHZ (H) | 44°17'42.58" / 9°45'44.36" | <15 cm | 15 cm | 38 | 44 | 13 | 3 | 0.1 | 1.5 | 0.58 | 0.19 | 0.18 | 0.04 |
| MC17A3 | LHZ (H) | 44°17'42.58" / 9°45'44.36" | <15 cm | >6 cm | | | | | | | | | | |
| MC17A4* | LHZ (W) | 44°17'42.58" / 9°45'44.36" | <5 cm | 3.2 cm | 33 | 39 | 24 | 3 | 0.3 | 0.9 | 0.72 | 0.13 | 0.23 | 0.03 |
| MC17A5* | LHZ (X) | 44°17'42.58" / 9°45'44.36" | <5 cm | 2.2 cm | 38 | 31 | 15 | 4 | 5.8 | 5.3 | 0.73 | 0.14 | 0.15 | 0.05 |
| | PYX (X) | | <3 cm | - | 3 | 32 | 40 | 2 | 6.9 | 15.7 | 0.45 | 0.02 | 0.12 | 0.05 |
| MC17A6 | PYX (P) | 44°17'42.58" / 9°45'44.36" | <8 cm | ~4 cm | 0.1 | 37 | 56 | 1 | 3.2 | 1.8 | 0.51 | 0.14 | 0.17 | 0.08 |
| MC17B1 | LHZ (H) ¹ | 44°17'42.58" / 9°45'44.36" | >2 m | >12 cm | | | | | | | | | | |
| MC17B2 | LHZ (H) ¹ | 44°17'42.58" / 9°45'44.36" | >2 m | >15 cm | | | | | | | | | | |
| MC17C2* | LHZ (W) | 44°17'42.58" / 9°45'44.36" | <3 cm | 2.8 cm | (10) | 26 | 49 | 3 | 4.1 | 8.0 | na | na | na | 0.03 |
| MC17C1 | HZB (H) | 44°17'42.58" / 9°45'44.36" | <8 cm | >6 cm | | | | | | | | | | |
| GV8A* | PYX (P) | 44°16'15.65" / 9°48'27.76" | <6 cm | - | 5 | 42 | 31 | 5 | 1.4 | 16.7 | 0.55 | 0.06 | 0.10 | 0.10 |
| GV8B* | LHZ (X) | 44°16'15.65" / 9°48'27.76" | <25 cm | 1 cm | 61 | 20 | 15 | 1 | 0.5 | 2.0 | 0.83 | 0.08 | 0.11 | 0.05 |
| | PYX (X) | | <6 cm | - | 6 | 89 | 1 | 1 | 0.3 | 2.1 | na | na | 0.18 | na |
| GV8W | LHZ (W) | 44°16'15.65" / 9°48'27.76" | <25 cm | 2 cm | 56 | 27 | 12 | 1 | 0.3 | 2.5 | 0.64 | 0.14 | 0.18 | 0.02 |
| GV8H | LHZ (H) | 44°16'15.65" / 9°48'27.76" | <25 cm | 6.5 cm | 63 | 17 | 14 | 1 | 0.3 | 4.3 | 0.69 | 0.11 | 0.15 | 0.05 |
| GV8HA* | LHZ (H) | 44°16'15.65" / 9°48'27.76" | <25 cm | 11.5 cm | 48 | 32 | 14 | 0 | 1.3 | 4.1 | 0.62 | 0.07 | 0.15 | 0.06 |
| GV8HB* | LHZ (H) | 44°16'15.65" / 9°48'27.76" | <25 cm | 16 cm | 51 | 29 | 11 | 0 | 2.0 | 7.1 | 0.53 | 0.05 | 0.13 | 0.11 |
| GV8HD | LHZ (H) | 44°16'15.65" / 9°48'27.76" | <25 cm | 20.5 cm | 52 | 29 | 12 | 1 | 0.8 | 4.4 | 0.70 | 0.10 | na | 0.07 |
| GV8D | LHZ (W) | 44°16'15.65" / 9°48'27.76" | <25 cm | >2 cm | | | | | | | | | | |
| GV10A | PYX (P) | 44°16'15.86" / 9°48'26.82" | <12 cm | - | 2 | 38 | 52 | 1 | 1.7 | 4.9 | 0.63 | 0.06 | 0.10 | 0.06 |
| GV10B | PYX (P) ² | 44°16'15.86" / 9°48'26.82" | <12 cm | - | 2 | 62 | 30 | 1 | 1.9 | 3.1 | na | na | 0.17 | 0.06 |
| BG13 | PYX (P) | 44°16'45.93" / 9°47'48.93" | <5 cm | - | (0) | (2) | 93 | 1 | 3.1 | (0) | na | na | na | 0.06 |
| BG13A* | LHZ (X) | 44°16'45.93" / 9°47'48.93" | | 1 cm | | | | | | | | | | |
| | PYX (X) | | <4 cm | - | 1 | 49 | 44 | 2 | 2.7 | 1.7 | 0.49 | 0.07 | 0.19 | 0.05 |
| BG13B* | LHZ (X) | 44°16'45.93" / 9°47'48.93" | | 1 cm | 50 | 30 | 17 | 1 | 0.1 | 0.7 | 0.93 | 0.09 | 0.21 | 0.03 |
| | PYX (X) | | <5 cm | - | 9 | 46 | 34 | 0 | 6.0 | 5.1 | 0.34 | 0.19 | 0.06 | 0.04 |
| BG14A | LHZ (W) | 44°16'44.15" / 9°47'50.15" | | 3 cm | 45 | 30 | 24 | 1 | 0.1 | 0.5 | 0.53 | 0.13 | 0.16 | 0.04 |
| BG14B* | PYX (P) | 44°16'44.15" / 9°47'50.15" | <5 cm | - | 8 | 65 | 26 | 1 | 0.1 | 0.4 | 0.59 | 0.05 | 0.13 | 0.07 |
| MC3 | LHZ (X) | 44°17'38.25" / 9°45'42.58" | | 1.5 cm | 53 | 29 | 11 | 1 | 1.1 | 5.5 | 0.83 | 0.16 | 0.04 | 0.03 |
| | PYX (X) | | <4 cm | - | 3 | 25 | 46 | 3 | 1.9 | 21.4 | 0.43 | 0.10 | 0.16 | 0.04 |
| MC5 | PYX (P) | 44°17'37.54" / 9°45'48.54" | <5 cm | - | 2 | 30 | 42 | 3 | 0.4 | 22.4 | 0.68 | 0.04 | 0.09 | 0.05 |

Column titles: t: thickness of the compositional layer; d: distance to nearest pyroxenite layer (or dunite in profile BG12); Amp: amphibole, Cpx: clinopyroxene, Ol: olivine; Opx: orthopyroxene; Pl: plagioclase; Spl: spinel; BA: BA-index describing the CPO symmetry of olivine; M(mineral abbreviation): Misorientation index describing the strength of CPO of a given mineral after Skemer et al. (2005).

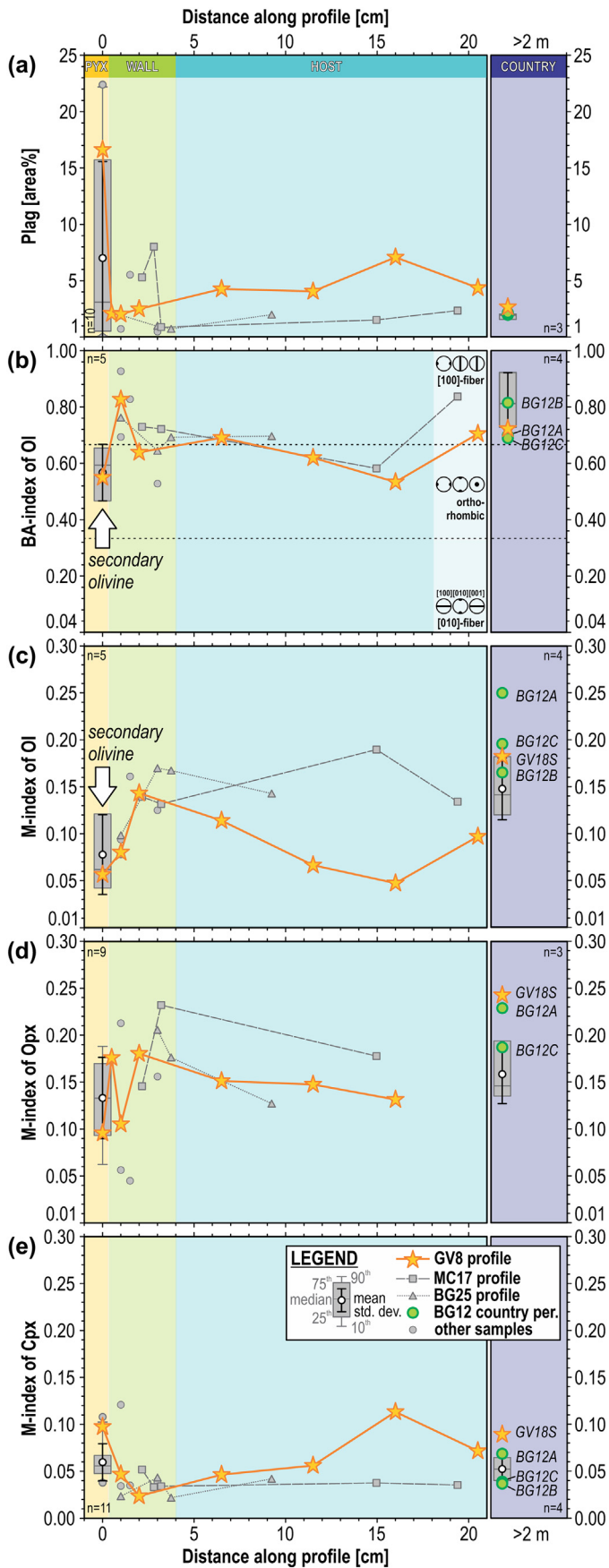
Other abbreviations: DUN: dunite; HZB: harzburgite; LHZ: lherzolite; PYX: pyroxenite; P: pyroxenite layer; X: composite sample; W: wallrock peridotite; H: host peridotite; C: country peridotite; na: not applicable, data has been omitted due to artifacts (see Supplementary Table S1 for the raw dataset). Number in a parenthesis at the modal composition indicates mineral mode highly distorted by alteration of the sample.

Annotations: 1: Cpx-poor; 2: Opx-rich rim; *: oriented sample.

Orientation data are presented in the pole figures in the structural reference frame, that is, relative to the orientation of the foliation and the lineation. For thin sections not cut normal to the foliation and parallel to the lineation, crystal orientation data have been rotated to this common structural frame for straightforward comparison between the different profiles. The data in the original thin section reference frame is displayed in the Supplementary Fig. S2. Pole figures in the manuscript are created using either the careware software package of David Mainprice (http://www.gm.univ-montp2.fr/PERSO/mainprice/W_data/CareWare_Unicef_Programs/, last access: January 2015), or built-in functions of MTEX. In the pole figures, all indexed pixels are preferred to the mean orientation of the grains (aka one-point per grain data) due to the alteration of the samples, if not otherwise indicated.

Mineral major element compositions were analyzed using: (1) a Philips SEM 515 equipped with an X-ray dispersive analyzer (accelerating potential 15 kV, beam current 20 nA), at the Dipartimento di Scienze della Terra, dell'Ambiente e della Vita, University of Genova, and (2) a JEOL JXA 8200 Superprobe equipped with five wavelength-dispersive (WDS) spectrometers, an energy dispersive (EDS) spectrometer, and a cathodoluminescence detector (accelerating potential 15 kV, beam current 15 nA), at the Dipartimento di Scienze della Terra, University of Milano. Representative mineral major element analyses are provided in Table 2 and the complete dataset is available in Supplementary Table S2.

In situ trace element mineral analyses were carried out by laser ablation microprobe - inductively coupled plasma mass spectrometry (LAM-ICPMS) at IGG-CNR, Pavia (Italy). The laser probe consisted of a



Q-switched Nd:YAG laser, model Quantel (Brilliant), whose fundamental emission in the near-IR region (1064 nm) was converted to 213 nm wavelength using three harmonic generators. The laser was operated at 10 Hz frequency, with a pulse energy of 35 mJ. Spot diameter was typically 50 μm . The ablated material was analyzed by using a PerkinElmer SCIEX ELAN DRC-e quadrupole mass spectrometer. Helium was used as carrier gas and mixed with Ar downstream of the ablation cell. We used NIST SRM 610 as external standard, and Ca as the internal standard for clinopyroxene. Data reduction was performed using the Glitter software. Repeated analyses of the BCR-2G reference material assessed the precision and accuracy of the data that resulted usually better than $\pm 10\%$.

5. Results

5.1. Petrography and microstructures

5.1.1. Peridotites

Country peridotites are dominantly lherzolite and harzburgite, but they can contain cm-wide dunite layers as well (Fig. 2a). Lithological boundaries, such as the lherzolite-dunite contact presented in Fig. 2a, are relatively sharp at the outcrop scale and subparallel to the plane of the foliation (Fig. 2a). These contacts are nevertheless irregular at the microscopic scale (Fig. 2b). Independently of modal composition, country peridotites have porphyroclastic textures. They are composed of coarse-grained (up to 5–7 mm in diameter), moderately elongated pyroxene (mostly orthopyroxene) and olivine porphyroclasts surrounded by smaller-sized, isometric olivine, pyroxenes, spinel (<4 mm), plagioclase (<2 mm) and amphibole (<1 mm) (Fig. 2b,d). Elongation of pyroxene porphyroclasts (aspect ratios up to 4) and alignment of isometric spinels in the plane of the foliation define a stretching lineation (Fig. 2a). The dunite layers display rare orthopyroxene porphyroclasts enclosed in a granoblastic, medium-sized (0.5–1 mm in diameter) olivine, pyroxenes, spinel and brownish amphibole assemblage (Fig. 2c). Clinopyroxene porphyroclasts are typically smaller than orthopyroxene ones (Fig. 2b–d). Orthopyroxene porphyroclasts have sutured grain boundaries with embayments filled with small olivine crystals (Fig. 2b,d). Olivine and pyroxene porphyroclasts display undulose extinction. In olivine, widely spaced subgrain boundaries perpendicular to the elongation direction are also observed (right inset in Fig. 2d). Porphyroclasts are often surrounded by neoblasts free from intracrystalline lattice distortion, recording recrystallization (Fig. 2b,d). However, strain-free, orthopyroxene neoblasts with interstitial habitus

Fig. 4. Compositional and microstructural variation across the studied pyroxenite-peridotite cross sections and in country peridotites: plagioclase modal composition (a), BA-index of olivine (b), and fabric strength of olivine (c), orthopyroxene (d) and clinopyroxene (e) expressed as the M-index (misorientation index of Skemer et al., 2005). Analytical artifacts distorting the results of the calculations have been omitted from the diagram; see Supplementary Table S1 for the unfiltered raw dataset. The most complete profile GV8 (see location in Fig. 3a–b) is highlighted with yellow stars, but data from profiles MC17 (gray square; see location in Fig. 1c) and BG25 (gray triangle; see location in Supplementary Fig. S1c–d) are also shown. For straightforward comparison, the origin is defined at the pyroxenite-peridotite contact and the zonation of wall rock and host peridotites that occur on both sides of the pyroxenite layer is displayed together, at the corresponding distance. For simplicity, in the pyroxenite layer and in the country peridotite only the central part of the sampling distribution is shown, where the lower boundary of the box indicates the 25th percentile, a line marks the median and the upper boundary of the box indicates the 75th percentile. Gray whiskers above and below the box, if displayed, indicate the 90th and 10th percentiles, respectively. White circle symbols with error bars outlined in black within the boxes indicate the means of sampling distribution with 1 σ standard deviation. Extreme values (i.e., outliers) in the field of pyroxenites and country peridotite in (a) and (e) are shown with gray circles. The country peridotite data from profile BG12 is displayed as green circles; see location in Fig. 2). The secondary olivine label in (b–c) is a reminder that most olivine in the pyroxenite layer is formed during the spinel-to plagioclase lherzolite-facies phase transformation reaction. (For interpretation of the references to color in this figure legend, the reader is referred to the web version of this article.)

Table 2
Representative major element composition of the main constituent minerals in the three new EL mantle profiles. See Supplementary Table S2 for the full dataset.

| Sample | BG12A (Dunite) | | | | BG12B (Dunite) | | | | BG12B (Lherzolite) | | | | BG12C (Lherzolite) | | | | BG25A (Lherzolite) | | | | BG25A (Dunite) | | | |
|--------------------------------|----------------|-------|-------|-------|----------------|-------|-------|-------|--------------------|-------|-------|-----|--------------------|-------|-------|-------|--------------------|-------|-------|-------|----------------|-------|-------|-------|
| | Ol | Opx | Cpx | Spl | Ol | Opx | Cpx | Spl | Ol | Opx | Cpx | Spl | Ol | Opx | Cpx | Spl | Ol | Opx | Cpx | Spl | Ol | Opx | Cpx | Spl |
| SiO ₂ | 40.3 | 54.5 | 51.6 | 0.06 | 41.3 | 55.3 | 51.5 | 0.03 | 41.2 | 54.8 | 51.3 | - | 41.2 | 55.2 | 51.0 | 0.02 | 41.4 | 55.3 | 51.2 | 0.01 | 41.8 | 55.0 | 51.1 | 0.02 |
| TiO ₂ | bdl | 0.14 | 0.41 | 0.08 | 0.03 | 0.17 | 0.47 | 0.09 | 0.02 | 0.07 | 0.69 | - | bdl | 0.14 | 0.63 | 0.25 | bdl | 0.11 | 1.02 | 0.16 | 0.03 | 0.22 | 0.95 | 0.08 |
| Al ₂ O ₃ | bdl | 4.73 | 5.90 | 53.0 | 0.02 | 4.64 | 6.55 | 52.8 | 0.02 | 5.38 | 6.46 | - | bdl | 5.30 | 7.71 | 50.1 | 0.01 | 4.97 | 7.13 | 53.1 | 0.01 | 5.58 | 7.25 | 53.7 |
| Cr ₂ O ₃ | bdl | 0.73 | 1.12 | 15.1 | bdl | 0.66 | 1.15 | 15.4 | 0.00 | 0.67 | 1.09 | - | bdl | 0.40 | 0.87 | 18.5 | bdl | 0.57 | 0.57 | 14.8 | bdl | 0.54 | 0.55 | 14.3 |
| FeO | 9.75 | 6.41 | 2.86 | 13.7 | 9.64 | 6.39 | 2.75 | 14.4 | 9.80 | 6.45 | 2.84 | - | 10.1 | 6.59 | 2.92 | 14.4 | 10.2 | 6.66 | 2.93 | 13.9 | 10.3 | 6.57 | 2.96 | 13.0 |
| MgO | 48.6 | 31.6 | 14.4 | 18.3 | 49.2 | 31.7 | 14.3 | 17.9 | 48.0 | 31.6 | 14.3 | - | 48.9 | 31.2 | 14.1 | 17.9 | 47.5 | 31.5 | 14.2 | 17.9 | 47.3 | 30.9 | 13.7 | 18.2 |
| MnO | 0.08 | 0.13 | 0.10 | 0.05 | 0.09 | 0.15 | 0.07 | 0.06 | 0.12 | 0.16 | 0.11 | - | 0.15 | 0.12 | 0.16 | 0.04 | 0.09 | 0.14 | 0.11 | 0.08 | 0.09 | 0.12 | 0.12 | 0.04 |
| NiO | 0.37 | 0.10 | 0.04 | 0.33 | 0.43 | 0.15 | 0.07 | 0.31 | 0.35 | 0.16 | 0.11 | - | 0.42 | 0.07 | 0.05 | 0.32 | 0.45 | 0.15 | 0.10 | 0.32 | 0.38 | 0.06 | 0.05 | 0.42 |
| CaO | 0.02 | 0.77 | 22.2 | bdl | 0.02 | 0.92 | 22.2 | 0.02 | 0.02 | 0.66 | 22.3 | - | 0.03 | 0.77 | 22.6 | 0.01 | 0.03 | 0.75 | 22.2 | bdl | 0.04 | 0.92 | 22.5 | bdl |
| Na ₂ O | bdl | 0.09 | 0.90 | bdl | bdl | 0.06 | 0.95 | bdl | 0.02 | 0.03 | 0.91 | - | 0.02 | 0.03 | 0.97 | 0.01 | 0.01 | 0.04 | 0.91 | bdl | 0.03 | 0.11 | 0.92 | bdl |
| K ₂ O | bdl | 0.01 | bdl | bdl | bdl | 0.01 | bdl | bdl | bdl | bdl | 0.01 | - | bdl | bdl | bdl | 0.01 | bdl | bdl | bdl | bdl | 0.01 | 0.01 | bdl | bdl |
| Total | 99.1 | 99.2 | 99.5 | 100.6 | 100.7 | 100.2 | 100.0 | 101.0 | 99.6 | 100.0 | 100.1 | - | 100.7 | 99.8 | 101.0 | 101.5 | 99.6 | 100.1 | 100.3 | 100.3 | 100.0 | 100.1 | 100.1 | 99.8 |
| Mg# | 0.899 | 0.898 | 0.900 | 0.725 | 0.901 | 0.898 | 0.902 | 0.708 | 0.90 | 0.897 | 0.900 | - | 0.897 | 0.894 | 0.896 | 0.712 | 0.893 | 0.894 | 0.896 | 0.697 | 0.891 | 0.893 | 0.892 | 0.715 |
| Cr# | - | 0.093 | 0.113 | 0.160 | - | 0.087 | 0.105 | 0.164 | - | 0.077 | 0.102 | - | - | 0.048 | 0.070 | 0.199 | - | 0.071 | 0.051 | 0.158 | - | 0.061 | 0.049 | 0.152 |

| Sample | BG25B (Lherzolite) | | | | BG25B (Dunite) | | | | BG25C (Lherzolite) | | | | BG25C (Pyroxenite) | | | | BG25D (Harzburgite) | | | | MC17A1 (Dunite) | | | |
|--------------------------------|--------------------|-------|-------|-------|----------------|-------|-------|-------|--------------------|-------|-------|-------|--------------------|-------|-------|-------|---------------------|-------|-------|-------|-----------------|-------|-------|-------|
| | Ol | Opx | Cpx | Spl | Ol | Opx | Cpx | Spl | Ol | Opx | Cpx | Spl | Ol | Opx | Cpx | Spl | Ol | Opx | Cpx | Spl | Ol | Opx | Cpx | Spl |
| SiO ₂ | 40.4 | 55.4 | 51.6 | 0.01 | 40.9 | 54.9 | 50.8 | bdl | 41.4 | 55.2 | 51.1 | bdl | - | 55.3 | 50.4 | 0.01 | 41.4 | 54.6 | 50.7 | 0.01 | 40.4 | 53.5 | 50.4 | 0.03 |
| TiO ₂ | 0.02 | 0.24 | 1.01 | 0.21 | bdl | 0.24 | 0.79 | 0.15 | bdl | 0.20 | 0.88 | 0.23 | - | 0.10 | 0.86 | 0.12 | 0.02 | 0.13 | 0.68 | 0.21 | 0.03 | 0.14 | 0.82 | 0.13 |
| Al ₂ O ₃ | bdl | 4.87 | 6.29 | 55.3 | 0.03 | 5.24 | 7.31 | 58.0 | bdl | 5.80 | 7.34 | 55.7 | - | 6.00 | 7.89 | 64.2 | bdl | 5.52 | 7.35 | 55.6 | 0.01 | 5.66 | 5.86 | 54.4 |
| Cr ₂ O ₃ | 0.03 | 0.38 | 0.70 | 13.56 | bdl | 0.44 | 0.76 | 9.85 | bdl | 0.35 | 0.61 | 12.25 | - | 0.35 | 0.40 | 4.15 | 0.02 | 0.42 | 0.90 | 13.6 | 0.01 | 0.52 | 0.88 | 13.1 |
| FeO | 10.4 | 6.93 | 2.82 | 13.5 | 10.4 | 7.04 | 3.17 | 12.2 | 10.7 | 6.94 | 3.21 | 13.5 | - | 7.14 | 3.30 | 11.6 | 10.7 | 6.70 | 3.09 | 13.4 | 10.1 | 6.59 | 2.78 | 12.7 |
| MgO | 48.6 | 31.7 | 14.5 | 18.9 | 48.1 | 31.2 | 14.2 | 18.9 | 47.4 | 31.4 | 14.0 | 18.3 | - | 31.2 | 13.9 | 20.1 | 47.7 | 31.3 | 13.7 | 18.4 | 48.7 | 31.3 | 14.8 | 19.5 |
| MnO | 0.15 | 0.18 | 0.11 | 0.04 | 0.20 | 0.16 | 0.13 | 0.09 | 0.15 | 0.20 | 0.13 | 0.05 | - | 0.20 | 0.11 | 0.09 | 0.15 | 0.16 | 0.05 | 0.09 | 0.10 | 0.11 | 0.11 | na |
| NiO | 0.40 | 0.09 | 0.00 | 0.33 | 0.37 | 0.14 | bdl | 0.35 | 0.34 | 0.01 | 0.02 | 0.38 | - | 0.05 | 0.12 | 0.49 | 0.34 | 0.06 | 0.05 | 0.35 | 0.30 | 0.05 | 0.09 | na |
| CaO | 0.03 | 0.69 | 22.6 | bdl | 0.01 | 0.68 | 22.2 | 0.01 | 0.04 | 0.79 | 22.1 | 0.01 | - | 0.56 | 22.6 | 0.02 | 0.01 | 0.65 | 22.5 | 0.01 | 0.03 | 0.70 | 21.9 | bdl |
| Na ₂ O | bdl | bdl | 0.92 | bdl | bdl | 0.05 | 0.83 | bdl | bdl | 0.03 | 0.81 | 0.01 | - | 0.02 | 0.86 | bdl | bdl | 0.02 | 0.80 | bdl | bdl | 0.04 | 0.83 | na |
| K ₂ O | bdl | bdl | 0.00 | bdl | 0.02 | bdl | bdl | bdl | 0.01 | bdl | bdl | bdl | - | 0.01 | 0.01 | 0.01 | bdl | 0.01 | 0.02 | bdl | 0.01 | bdl | bdl | na |
| Total | 100.1 | 100.4 | 100.6 | 101.8 | 100.1 | 100.2 | 100.2 | 99.6 | 100.0 | 100.8 | 100.1 | 100.4 | - | 100.9 | 100.4 | 100.8 | 100.3 | 99.5 | 99.9 | 101.7 | 99.7 | 98.6 | 98.5 | 99.9 |
| Mg# | 0.893 | 0.891 | 0.902 | 0.714 | 0.892 | 0.888 | 0.889 | 0.735 | 0.888 | 0.890 | 0.886 | 0.706 | - | 0.886 | 0.882 | 0.757 | 0.888 | 0.893 | 0.888 | 0.711 | 0.896 | 0.894 | 0.905 | 0.732 |
| Cr# | - | 0.050 | 0.069 | 0.141 | - | 0.054 | 0.065 | 0.102 | - | 0.039 | 0.053 | 0.128 | - | 0.037 | 0.033 | 0.042 | - | 0.049 | 0.076 | 0.141 | - | 0.058 | 0.092 | 0.136 |

| Sample | MC17A2 (Lherzolite) | | | | MC17A3 (Lherzolite) | | | | MC17A4 (Lherzolite) | | | | MC17A1 (Dunite) | | | | MC17A2 (Lherzolite) ¹ | | | | MC17A3 (Lherzolite) ¹ | | | |
|--------------------------------|---------------------|------|------|------|---------------------|------|------|------|---------------------|------|------|------|-----------------|------|------|------|----------------------------------|------|------|------|----------------------------------|------|------|------|
| | Ol | Opx | Cpx | Spl | Ol | Opx | Cpx | Spl | Ol | Opx | Cpx | Spl | Ol | Opx | Cpx | Spl | Ol | Opx | Cpx | Spl | Ol | Opx | Cpx | Spl |
| SiO ₂ | 40.8 | 54.1 | 49.8 | 0.06 | 40.5 | 53.7 | 50.2 | 0.04 | 40.4 | 53.8 | 49.9 | 0.02 | 40.4 | 53.5 | 50.4 | 0.03 | 40.8 | 54.1 | 49.8 | 0.06 | 40.5 | 53.7 | 50.2 | 0.04 |
| TiO ₂ | bdl | 0.16 | 0.83 | 0.22 | 0.05 | 0.21 | 0.97 | 0.19 | bdl | 0.26 | 0.94 | 0.22 | 0.03 | 0.14 | 0.82 | 0.13 | bdl | 0.16 | 0.83 | 0.22 | 0.05 | 0.21 | 0.97 | 0.19 |
| Al ₂ O ₃ | 0.02 | 5.36 | 7.60 | 55.6 | bdl | 5.84 | 6.68 | 54.4 | bdl | 5.59 | 7.90 | 52.5 | 0.01 | 5.66 | 5.86 | 54.4 | 0.02 | 5.36 | 7.60 | 55.6 | bdl | 5.84 | 6.68 | 54.4 |

(continued on next page)

Table 2 (continued)

| Sample | MC17A2 (Lherzolite) | | | | MC17A3 (Lherzolite) | | | | MC17A4 (Lherzolite) | | | | MC17A1 (Dunite) | | | | MC17A2 (Lherzolite) ¹ | | | | MC17A3 (Lherzolite) ¹ | | | |
|--------------------------------|---------------------|-------|-------|-------|---------------------|-------|-------|-------|---------------------|-------|-------|-------|-----------------|-------|-------|-------|----------------------------------|-------|-------|-------|----------------------------------|-------|-------|-------|
| | Ol | Opx | Cpx | Spl | Ol | Opx | Cpx | Spl | Ol | Opx | Cpx | Spl | Ol | Opx | Cpx | Spl | Ol | Opx | Cpx | Spl | Ol | Opx | Cpx | Spl |
| Cr ₂ O ₃ | bdl | 0.49 | 0.73 | 11.9 | bdl | 0.44 | 0.78 | 13.5 | 0.03 | 0.32 | 0.80 | 14.8 | 0.01 | 0.52 | 0.88 | 13.1 | bdl | 0.49 | 0.73 | 11.9 | bdl | 0.44 | 0.78 | 13.5 |
| FeO | 10.7 | 6.85 | 2.94 | 13.2 | 10.8 | 7.29 | 3.11 | 14.1 | 11.3 | 7.47 | 3.35 | 14.8 | 10.1 | 6.59 | 2.78 | 12.7 | 10.7 | 6.85 | 2.94 | 13.2 | 10.8 | 7.29 | 3.11 | 14.1 |
| MgO | 49.2 | 32.2 | 14.1 | 18.6 | 48.7 | 32.0 | 14.8 | 18.6 | 47.9 | 31.8 | 14.3 | 17.6 | 48.7 | 31.3 | 14.8 | 19.5 | 49.2 | 32.2 | 14.1 | 18.6 | 48.7 | 32.0 | 14.8 | 18.6 |
| MnO | 0.20 | 0.21 | 0.03 | na | 0.17 | 0.16 | 0.06 | na | 0.19 | 0.14 | 0.08 | na | 0.10 | 0.11 | 0.11 | na | 0.20 | 0.21 | 0.03 | na | 0.17 | 0.16 | 0.06 | na |
| NiO | 0.42 | 0.12 | bdl | na | 0.42 | 0.13 | 0.02 | na | 0.32 | 0.06 | 0.03 | na | 0.30 | 0.05 | 0.09 | na | 0.42 | 0.12 | bdl | na | 0.42 | 0.13 | 0.02 | na |
| CaO | 0.04 | 0.64 | 22.5 | bdl | 0.04 | 0.60 | 22.1 | bdl | 0.03 | 0.55 | 22.0 | 0.01 | 0.03 | 0.70 | 21.9 | bdl | 0.04 | 0.64 | 22.5 | bdl | 0.04 | 0.60 | 22.1 | bdl |
| Na ₂ O | bdl | 0.02 | 0.96 | na | 0.01 | 0.01 | 0.79 | na | bdl | 0.03 | 0.86 | na | bdl | 0.04 | 0.83 | na | bdl | 0.02 | 0.96 | na | 0.01 | 0.01 | 0.79 | na |
| K ₂ O | 0.01 | bdl | bdl | na | bdl | bdl | 0.01 | na | bdl | 0.01 | bdl | na | 0.01 | bdl | bdl | na | 0.01 | bdl | bdl | na | bdl | bdl | 0.01 | na |
| Total | 101.4 | 100.1 | 99.5 | 99.6 | 100.7 | 100.4 | 99.5 | 100.8 | 100.1 | 100.0 | 100.2 | 100.0 | 99.7 | 98.6 | 98.5 | 99.9 | 101.4 | 100.1 | 99.5 | 99.6 | 100.7 | 100.4 | 99.5 | 100.8 |
| Mg# | 0.891 | 0.893 | 0.896 | 0.716 | 0.889 | 0.887 | 0.895 | 0.723 | 0.884 | 0.883 | 0.884 | 0.680 | 0.896 | 0.894 | 0.905 | 0.732 | 0.891 | 0.893 | 0.896 | 0.716 | 0.889 | 0.887 | 0.895 | 0.723 |
| Cr# | - | 0.058 | 0.060 | 0.125 | - | 0.048 | 0.073 | 0.143 | - | 0.037 | 0.064 | 0.157 | - | 0.058 | 0.092 | 0.136 | - | 0.058 | 0.060 | 0.125 | - | 0.048 | 0.073 | 0.143 |

| Sample | MC17A4 (Lherzolite) | | | | MC17A6 (Pyroxenite) | | | | MC17B1 (Lherzolite) | | | | MC17B2 (Lherzolite) ¹ | | | | MC17C1 (Harzburgite) | | | |
|--------------------------------|---------------------|-------|-------|-------|---------------------|-------|-------|-------|---------------------|-------|-------|-------|----------------------------------|-------|-------|-------|----------------------|-------|-------|-------|
| | Ol | Opx | Cpx | Spl | Ol | Opx | Cpx | Spl | Ol | Opx | Cpx | Spl | Ol | Opx | Cpx | Spl | Ol | Opx | Cpx | Spl |
| SiO ₂ | 40.4 | 53.8 | 49.9 | 0.02 | - | 53.6 | 48.8 | 0.06 | 40.5 | 53.8 | 52.2 | 0.06 | 40.4 | 54.5 | 50.3 | 0.10 | 40.9 | 53.5 | 49.5 | bdl |
| TiO ₂ | bdl | 0.26 | 0.94 | 0.22 | - | 0.30 | 1.11 | 0.18 | 0.02 | 0.13 | 0.62 | 0.23 | 0.04 | 0.12 | 0.61 | 0.16 | bdl | 0.20 | 1.08 | 0.29 |
| Al ₂ O ₃ | bdl | 5.59 | 7.90 | 52.5 | - | 5.33 | 8.61 | 63.7 | bdl | 5.78 | 5.61 | 50.1 | 0.02 | 4.94 | 7.34 | 57.9 | bdl | 5.87 | 6.79 | 51.4 |
| Cr ₂ O ₃ | 0.03 | 0.32 | 0.80 | 14.8 | - | 0.17 | 0.10 | 2.56 | 0.02 | 0.54 | 0.88 | 17.5 | 0.01 | 0.47 | 0.80 | 9.76 | 0.01 | 0.37 | 0.66 | 15.9 |
| FeO | 11.3 | 7.47 | 3.35 | 14.8 | - | 9.15 | 4.35 | 14.5 | 9.57 | 6.25 | 2.87 | 13.6 | 9.42 | 6.40 | 2.77 | 12.1 | 10.3 | 7.42 | 2.97 | 15.8 |
| MgO | 47.9 | 31.8 | 14.3 | 17.6 | - | 30.7 | 13.7 | 18.8 | 48.8 | 32.0 | 14.9 | 17.6 | 49.4 | 32.4 | 14.7 | 19.2 | 48.4 | 31.5 | 14.3 | 17.3 |
| MnO | 0.19 | 0.14 | 0.08 | na | - | 0.24 | 0.17 | | 0.13 | 0.09 | 0.04 | na | 0.16 | 0.11 | 0.11 | na | 0.18 | 0.15 | 0.05 | na |
| NiO | 0.32 | 0.06 | 0.03 | na | - | 0.13 | 0.09 | | 0.36 | 0.11 | 0.07 | na | 0.22 | 0.15 | 0.04 | na | 0.41 | 0.07 | bdl | na |
| CaO | 0.03 | 0.55 | 22.0 | 0.01 | - | 0.74 | 21.9 | bdl | 0.03 | 0.70 | 22.5 | 0.01 | 0.04 | 0.55 | 21.8 | 0.02 | 0.02 | 0.76 | 22.1 | 0.02 |
| Na ₂ O | bdl | 0.03 | 0.86 | na | - | 0.05 | 0.86 | | 0.02 | 0.04 | 0.78 | na | bdl | 0.05 | 0.76 | na | bdl | 0.01 | 0.80 | na |
| K ₂ O | bdl | 0.01 | bdl | na | - | 0.01 | bdl | | 0.01 | 0.01 | bdl | na | bdl | 0.01 | bdl | na | bdl | 0.01 | bdl | na |
| Total | 100.1 | 100.0 | 100.2 | 100.0 | - | 100.4 | 99.6 | 99.7 | 99.5 | 99.4 | 100.5 | 99.2 | 99.7 | 99.7 | 99.2 | 99.3 | 100.2 | 99.9 | 98.4 | 100.7 |
| Mg# | 0.884 | 0.883 | 0.884 | 0.680 | - | 0.857 | 0.848 | 0.698 | 0.901 | 0.901 | 0.903 | 0.697 | 0.903 | 0.900 | 0.905 | 0.739 | 0.894 | 0.883 | 0.896 | 0.661 |
| Cr# | - | 0.037 | 0.064 | 0.157 | - | 0.021 | 0.008 | 0.026 | - | 0.059 | 0.095 | 0.188 | - | 0.060 | 0.068 | 0.101 | - | 0.040 | 0.061 | 0.168 |

Cpx: clinopyroxene; Ol: olivine; Opx: orthopyroxene; Spl: spinel. Cr# = Cr/(Cr + Al); Mg# = Mg/(Mg + Fe). 1: Cpx-poor; bdl: below detection limit; na: not analyzed.

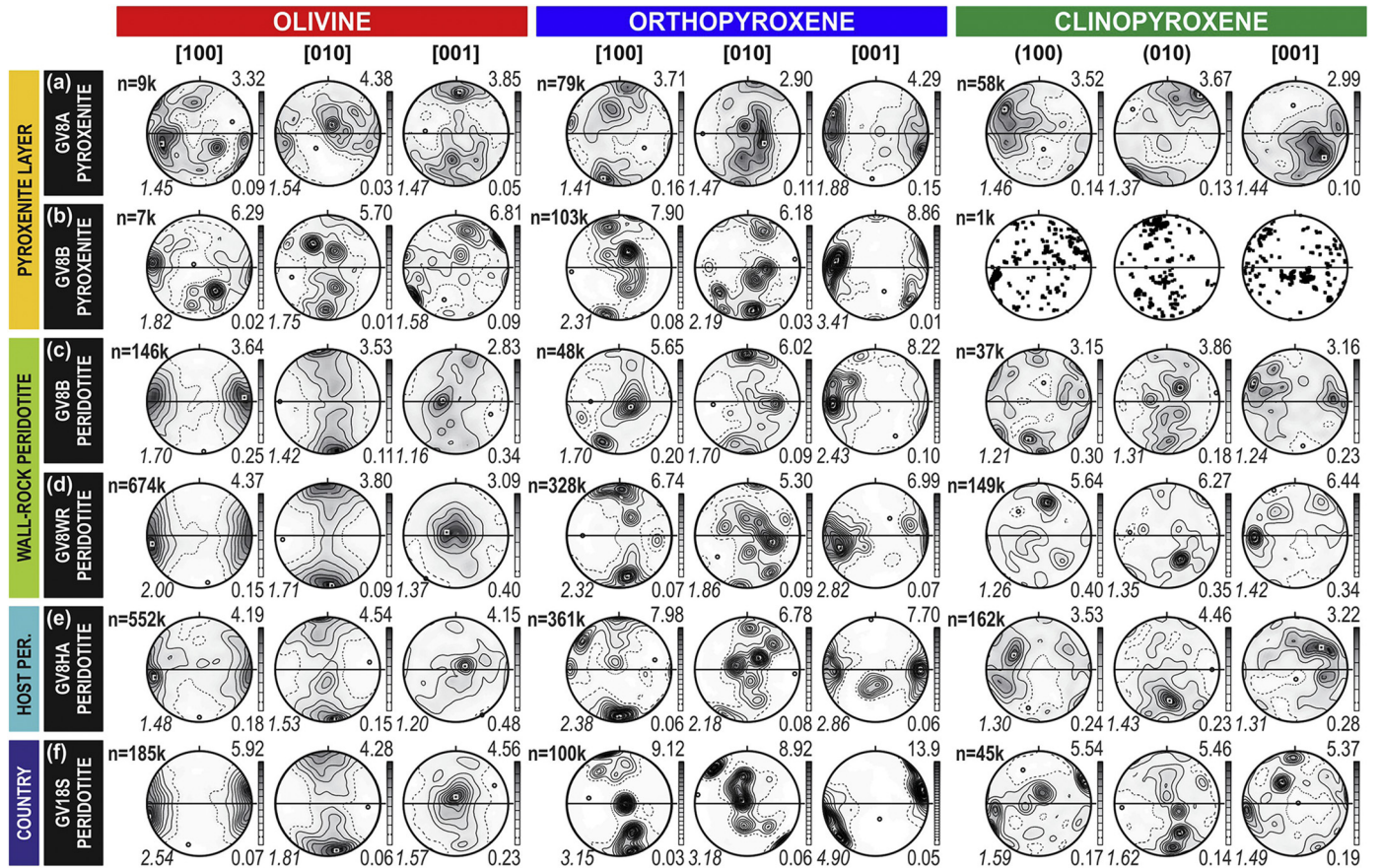


Fig. 5. CPO of olivine, orthopyroxene and clinopyroxene in representative members of the pyroxenite-peridotite profile GV8 (see Fig. 3 for location of samples). Due to non-perfect orientation of some thin sections, the EBSD data have been rotated to the common structural frame, which also allows direct comparison of CPO to that of the country peridotites (Fig. 2). See text for further details on this rotation. Pole figure plotting convention is the same as for Fig. 2.

also occur along anastomosing bands subparallel to the plane of the foliation (Fig. 2b,d). These bands are enriched in pyroxenes and plagioclase compared to the surrounding peridotite. Minerals in the fine-grained bands are moderately elongated (aspect ratios are up to 2) and their elongation direction is subparallel to that of the porphyroclasts.

With respect to the country peridotites, wall-rock and, in a lesser extent, host peridotites are characterized by pyroxene enrichment (mostly orthopyroxene) (Fig. 3d–g; samples BG14A,B in Supplementary Fig. S2), which is usually testified by the occurrence of large blebs of orthopyroxene and hunter-green spinel, as described by Borghini et al. (2020). Dunitic compositions are rare and, if occur, they are restricted to the distal domains of the host peridotite, far from the pyroxenite layers (e.g., sample BG25A, Supplementary Fig. S1d). Microstructural features of wall-rock and host peridotites are essentially the same as that of the country peridotites (Fig. 3h–l), but the former show a higher amount of fine-grained, pyroxene- and plagioclase-enriched bands with respect to the country peridotites (Fig. 3c–f and Supplementary Fig. S2).

Partial re-equilibration at plagioclase-facies conditions is indicated by i) thin rims of plagioclase and olivine crystallized around coarse brown to dark-brown spinels (up to 1–2 mm) (Fig. 3f), ii) plagioclase plus orthopyroxene exsolutions in large clinopyroxene porphyroclasts, iii) fine-grained (~200–300 μm in diameter) granoblastic aggregates made of plagioclase, olivine, pyroxenes, and occasionally Cr-rich spinel, developed between coarse porphyroclasts of spinel-facies pyroxenes (Fig. 2b, Fig. 3e,f). The amount of plagioclase is mostly controlled by the fertility of whole rock composition. In general, re-equilibration at plagioclase-facies conditions is well developed in lherzolites and only incipient in harzburgites. Plagioclase is not observed in dunites. Partial

re-equilibration at plagioclase-facies conditions shows no correlation with the distance to the pyroxenite layers (Fig. 4a). However, among lherzolites, plagioclase is more abundant within fine-grained pyroxene-rich bands of the wall rock and host peridotites.

Amphibole occurs as an accessory mineral, typically in textural contact with pyroxenes. Its modal abundance slightly increases towards the pyroxenite-peridotite contacts from typical values <0.5 area% in the country peridotites up to 0.5–1.3 area% in wall rocks and host peridotites (Table 1). Rare brown amphiboles occur dispersed in the country peridotites.

5.1.2. Pyroxenites

Pyroxenites are clinopyroxene-rich websterites (e.g., samples BG13A, GV8A, MC17A6) or clinopyroxenites (samples BG13 and BG14). They show a well-defined contact with the wall-rock peridotite, which is subparallel (<20°) to the peridotite foliation (Fig. 1c, 3d, Supplementary Fig. S2). However, at the cm to mm scale the contact is irregular (Fig. 3d; samples BG13A,B and BG25C in Supplementary Fig. S2). At the contact with the peridotite, pyroxenites are sometimes enriched in orthopyroxene that may form monomineralic rims up to 1 cm thick, as observed in samples GV8B (Fig. 3d) or BG14B (Supplementary Fig. S2). In these rims, orthopyroxene crystals are up to 5 mm in diameter, weakly elongated or equant in shape (Fig. 3i), have irregular grain boundaries, and display rare subgrains. The contact between the orthopyroxene-rich rim and the pyroxenite, defined by the appearance of clinopyroxene, is irregular at the cm to mm scale.

Away from the orthopyroxene-rich rims, pyroxenites are mainly composed of coarse-grained (0.5–1 cm), irregularly shaped clinopyroxene and orthopyroxene, and fine-grained (<0.3 mm) spinel

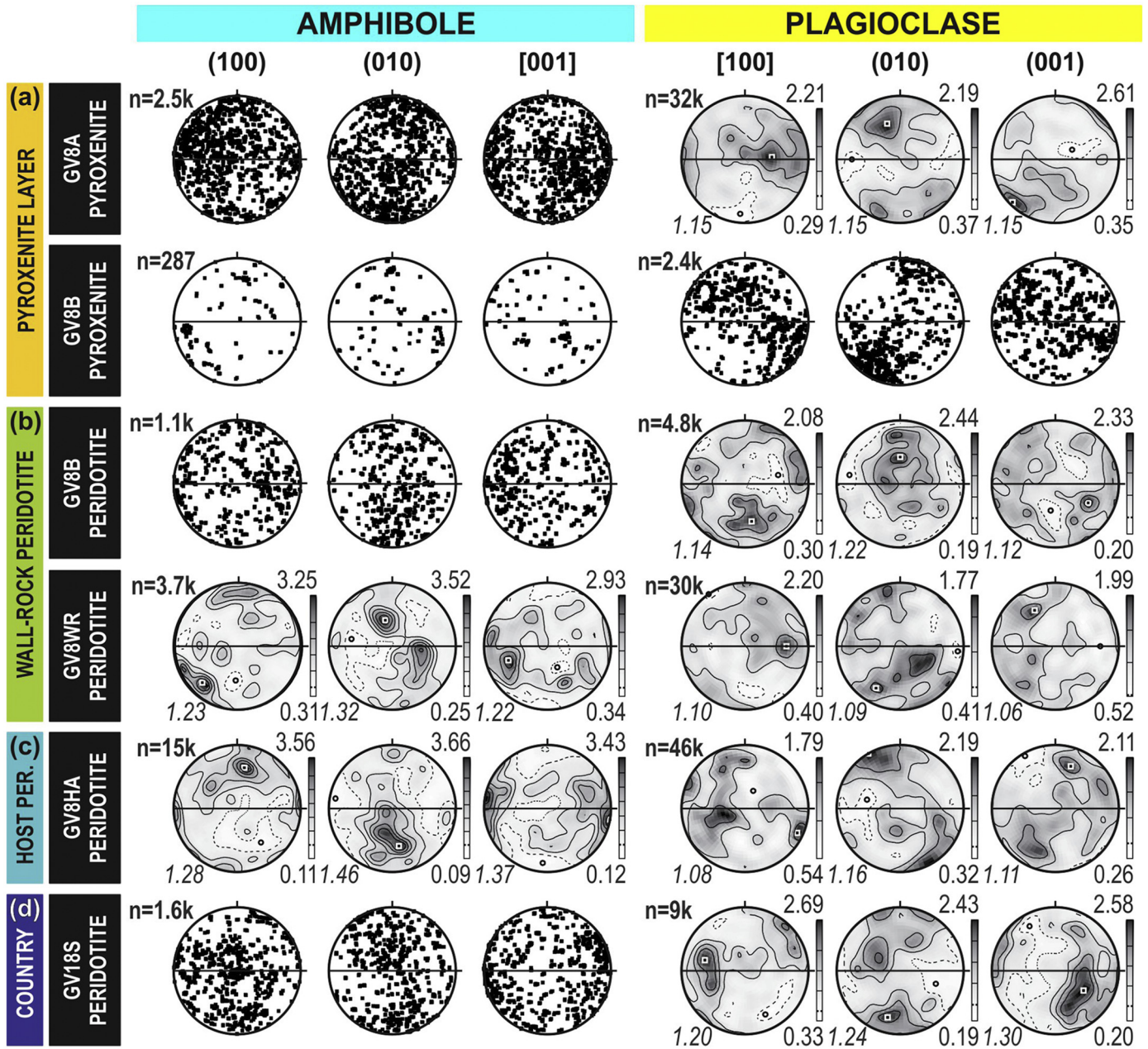


Fig. 6. CPO of amphibole and plagioclase accessory phases in representative members of the pyroxenite-peridotite profile GV8 (see Fig. 3 for location of samples). Details of data visualization are provided at Figs. 2 and 5.

(Fig. 3c,h). Orthopyroxene is usually the coarsest phase. It is weakly elongated (aspect ratios <1.5) subparallel to the layer and has often very sinuous grain boundaries (Fig. 3c,h). Clinopyroxene also has sinuous grain boundaries, but rather equant grain shapes. Clinopyroxene grain interiors are usually strain free (Fig. 3h), but rare subgrain boundaries and minor lattice distortion can be present close to the grain edges. Exsolution lamellae of orthopyroxene in clinopyroxene are observed only in the largest clinopyroxene grains.

Similar to fertile peridotites, pyroxenite layers also record subsolidus plagioclase-facies re-equilibration, which resulted in crystallization of plagioclase and increase of olivine content in the previously plagioclase-free and olivine-poor spinel-facies pyroxenite. Owing to their more fertile whole-rock composition (e.g. higher Al_2O_3 , CaO and Na_2O contents, Borghini et al., 2016), pyroxenite layers show more extensive subsolidus plagioclase-facies re-equilibration than the

peridotite in which they are embedded (Fig. 4a, Table 1). Locally, the plagioclase-facies assemblage occurs as fine-grained (0.3–0.4 mm in diameter) domains composed by intermixed olivine and plagioclase oriented subparallel to the peridotite foliation (Fig. 3c). Amphibole modal abundances are significantly higher in the pyroxenite layers than in the surrounding peridotites (typically >1.5 area%; Table 1). Amphibole typically occurs rimming both pyroxenes, but it also forms alignments within orthopyroxene porphyroclasts, supposedly corresponding to former clinopyroxene exsolution lamellae.

5.2. Crystallographic preferred orientation (CPO)

5.2.1. Peridotites

In the peridotites, olivine and pyroxenes display well-developed CPO (Figs. 2, 5). In composite thin sections containing two peridotite

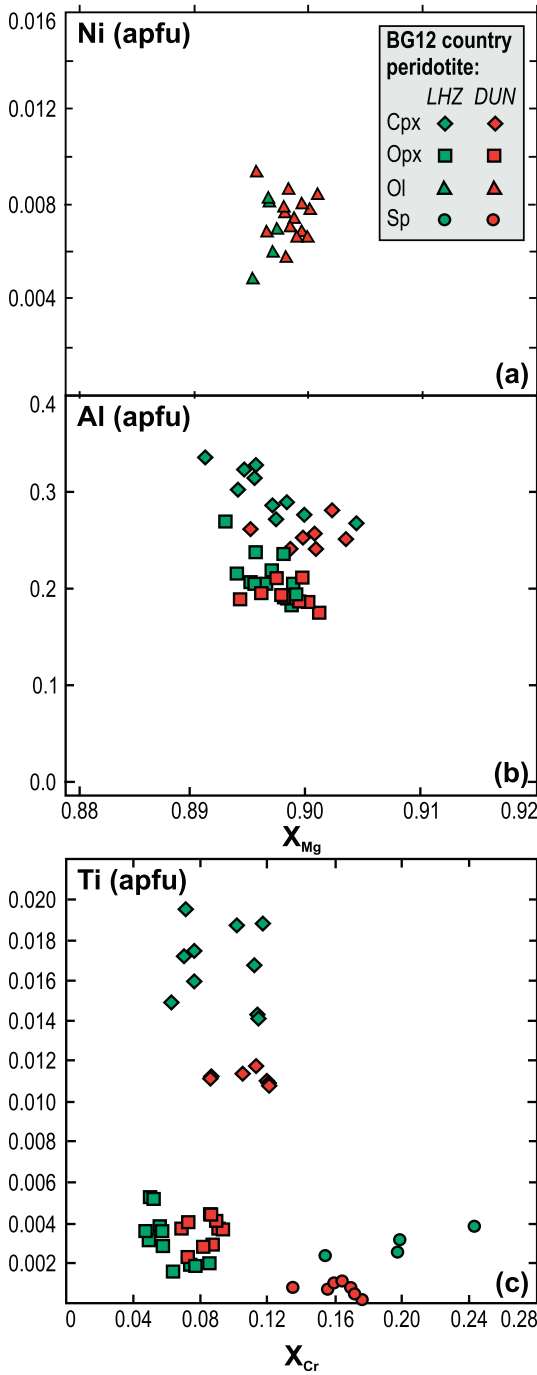


Fig. 7. Ni vs. X_{Mg} (a), Al vs. X_{Mg} (b) and Ti vs. X_{Cr} (c) mineral major element geochemical variation in the pyroxenite-free profile BG12, representative of country peridotites. apfu: atoms per formula unit. $X_{Mg} = Mg/(Mg + Fe^{2+})$ and $X_{Cr} = Cr/(Cr + Al)$, expressed as cation numbers.

lithologies (e.g., the lherzolite-dunite contact in Fig. 2b), there is no significant difference in the CPOs across the contact.

Olivine CPO in all peridotites is characterized by orthorhombic to axial-[100] symmetries (BA-index = 0.44–0.88). Olivine [100] is parallel to the lineation marked by the elongation of the porphyroclasts and the maximum density of [010] is roughly normal to the foliation plane (Figs. 2, 5c–f). In samples with axial-[100] olivine CPO symmetries, the [010]- and [001] axes show a continuous or discontinuous girdle perpendicular to the lineation. The olivine CPO symmetry does not show any systematic variation as a function of the distance to the pyroxenite layers (Fig. 4b). In contrast, the strength of the olivine CPO is the highest

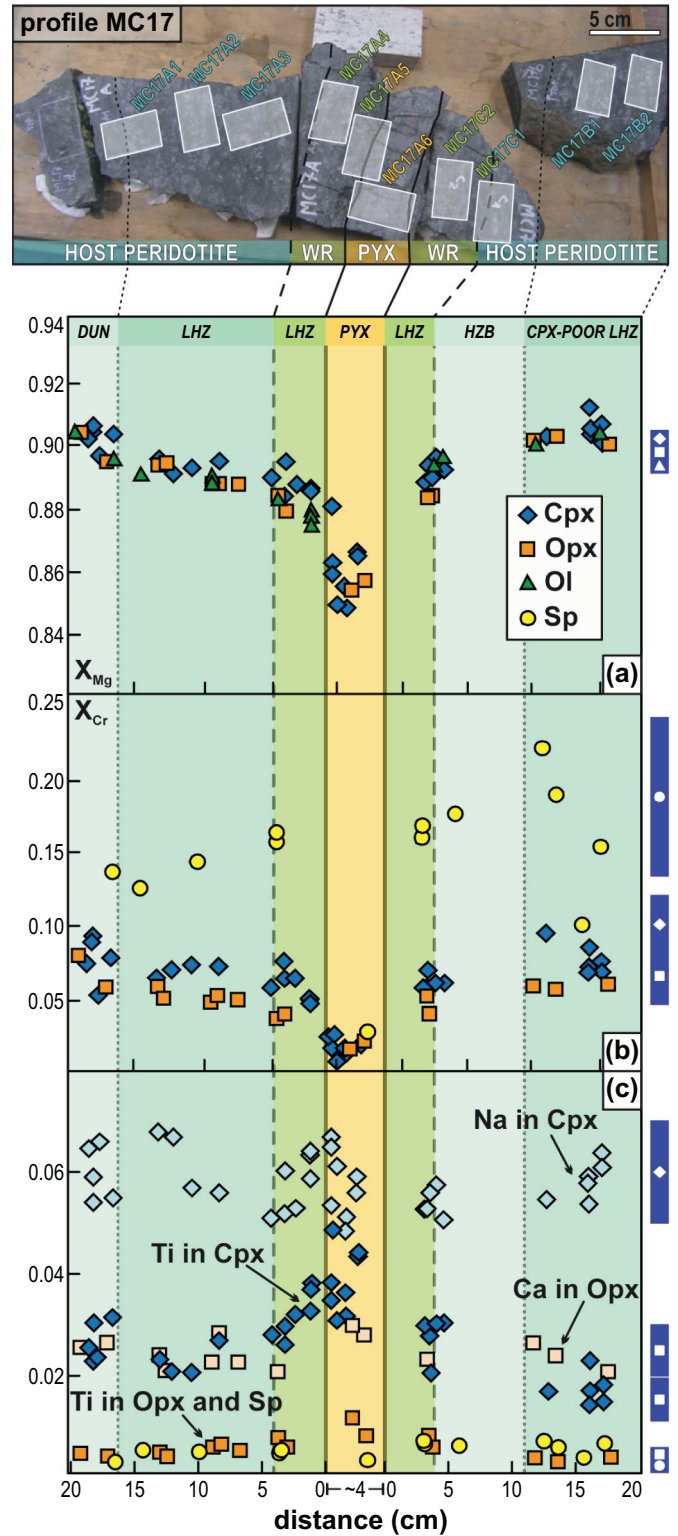


Fig. 8. Representative major element geochemical variation of the main constituent minerals across the ca. 45 cm long pyroxenite-peridotite profile MC17 (see Fig. 1c for location). The compositional range of country peridotites is shown on the right as blue boxes with symbols to the corresponding minerals. Cpx: clinopyroxene; Ol: olivine; Opx: orthopyroxene; Sp: Spinel. DUN: dunite; LHZ: lherzolite; HZB: harzburgite; PYX: pyroxenite; WR: wall-rock peridotite. $X_{Mg} = Mg/(Mg + Fe^{2+})$ and $X_{Cr} = Cr/(Cr + Al)$, expressed as cation numbers. (For interpretation of the references to color in this figure legend, the reader is referred to the web version of this article.)

in the country peridotites with M-index values of 0.16–0.25 (Fig. 4c) and it is usually weaker in the host peridotite (M-index: 0.05–0.19).

Table 3
Trace element composition of clinopyroxene in different lithologies of the profiles MC17 and BG12.

| Profile | MC17 | | | | | | BG12 | |
|----------------------------------|----------|-----------|------------|-------------|---------------------|--------|------------|---------|
| | Position | wallrock | | | host | | | country |
| | | Lithology | Lherzolite | Harzburgite | Cpx-poor lherzolite | | Lherzolite | Dunite |
| | | | Pyroxenite | MC17A4 | MC17C1 | MC17B1 | MC17B2 | MC17A1 |
| Sample | MC17A5 | MC17A4 | MC17C1 | MC17B1 | MC17B2 | MC17A1 | BG12A | |
| Sr | 4.45 | 21.9 | 16.8 | 13.8 | 23.8 | 13.5 | 48.1 | |
| Zr | 74.1 | 61.5 | 45.0 | 36.5 | 30.6 | 53.8 | 39.2 | |
| La | 0.62 | 0.89 | 0.80 | 0.60 | 0.69 | 0.72 | 1.11 | |
| Ce | 3.69 | 4.74 | 4.51 | 3.31 | 3.10 | 3.90 | 3.77 | |
| Pr | 1.04 | 1.01 | 1.15 | 0.70 | 0.68 | 0.94 | 0.72 | |
| Nd | 7.64 | 7.15 | 7.15 | 4.66 | 4.69 | 6.13 | 4.52 | |
| Sm | 4.07 | 2.95 | 2.85 | 2.05 | 2.05 | 2.66 | 1.64 | |
| Eu | 1.56 | 1.14 | 1.15 | 0.88 | 0.85 | 1.09 | 0.70 | |
| Gd | 6.82 | 4.03 | 4.13 | 3.30 | 2.91 | 4.23 | 2.33 | |
| Tb | 1.35 | 0.74 | 0.69 | 0.59 | 0.55 | 0.84 | 0.41 | |
| Dy | 9.52 | 4.77 | 4.35 | 4.19 | 3.67 | 5.66 | 2.82 | |
| Ho | 2.23 | 1.07 | 0.97 | 0.95 | 0.85 | 1.32 | 0.61 | |
| Er | 6.39 | 2.93 | 2.67 | 2.74 | 2.41 | 3.32 | 1.64 | |
| Tm | 0.97 | 0.42 | 0.40 | 0.39 | 0.36 | 0.51 | 0.21 | |
| Yb | 6.51 | 2.55 | 2.65 | 2.61 | 2.31 | 3.10 | 1.37 | |
| Lu | 0.97 | 0.36 | 0.40 | 0.36 | 0.35 | 0.46 | 0.18 | |
| La _N /Sm _N | 0.10 | 0.19 | 0.18 | 0.18 | 0.21 | 0.17 | 0.42 | |
| La _N /Yb _N | 0.07 | 0.24 | 0.21 | 0.16 | 0.21 | 0.16 | 0.56 | |
| Sm _N /Yb _N | 0.69 | 1.28 | 1.19 | 0.87 | 0.98 | 0.95 | 1.32 | |

The strength of the olivine CPO may show a slight increase in the wall-rock peridotite (M-index: 0.05–0.23), but strongly decreases at the contact with the pyroxenite layer (Fig. 4c).

Orthopyroxene CPO is usually coherent with that of olivine, that is, the maxima of [001]_{OPX} and [100]_{OPX} axes are subparallel to the maxima of [100]_{Ol} and [010]_{Ol}, respectively (Fig. 2b–d, 5c–f). There is a small obliquity between the olivine and orthopyroxene CPO, which is commonly observed in naturally deformed mantle peridotites worldwide (e.g., Cao et al., 2015; Fernández-Roig et al., 2017; Frets et al., 2012; Frets et al., 2014; Le Roux et al., 2008; Puziewicz et al., 2020; Tommasi et al., 2004; Tommasi et al., 2006). Clinopyroxene CPO is more dispersed than that of olivine and orthopyroxene. However, a weak correlation exists between clinopyroxene [001]_{CPX}, [100]_{Ol}, and [001]_{OPX} maxima, which are always oriented at low angle to the lineation, marked by the weak elongation of this phase as well as olivine and orthopyroxene porphyroclasts (Fig. 2b–d, 5c–f). The (010)_{CPX} planes are subparallel to (010)_{Ol}, and their maxima tend to be at high angle to the foliation (Fig. 2b–d, 5b–d). As for olivine, the strength of orthopyroxene CPO is on average higher in the country peridotites (M-index of 0.16–0.25; Fig. 4d). Along a specific cross section, the orthopyroxene CPO strength is usually weaker in the host peridotite far from the contact (M-index: 0.05–0.19) and it is highly variable in the wall rock close to the contact with the pyroxenite, ranging between very weak (M-index as low as 0.05) to moderate-strong (M-index up to 0.23) (Fig. 4d). In contrast, the M-index of clinopyroxene is rather constant indicating a uniformly weak CPO (M-index <0.15) (Fig. 4e).

Among the accessory phases, amphibole CPO typically mimics that of either clinopyroxene or orthopyroxene in a given peridotite sample (Fig. 6). Plagioclase in most of the cases has a weak CPO with the pole of (010) typically at high angle to the foliation (Fig. 6).

5.2.2. Pyroxenite layers

Olivine CPO in the pyroxenite layers is on average more dispersed than in peridotites (Fig. 4c), but a quantitative description is hindered by the low modal amount of this phase. Statistically significant number of grains was analyzed only in the olivine- and plagioclase-rich bands, which record the re-equilibration to plagioclase-facies. In these domains, olivine is weakly oriented with the [100]_{Ol} axes subparallel to the bands orientation and [001]_{Ol} axes at high angle to it (Fig. 5a–b).

The CPO of pyroxenes is also on average more dispersed in the pyroxenites than in the peridotites, as indicated by their weaker

M-index (typically <0.17 for orthopyroxene and < 0.10 in clinopyroxene) (Fig. 4c–e). In composite thin sections containing the pyroxenite and wall rock peridotite, the CPO of orthopyroxene and clinopyroxene are similar in the two lithologies (Fig. 5b vs. 5c). The clinopyroxene CPO is usually more dispersed than that of orthopyroxene. However, the maximum density of (010)_{CPX} tends to be oriented roughly normal to the contact with the peridotite and to the foliation in the wall rock and host peridotite (Fig. 5a–b).

As in the peridotites, amphibole CPO is similar to that of orthopyroxene or clinopyroxene in a given sample (Fig. 6). Plagioclase CPO is weak, but the maximum density of the pole to (010)_{Pl} is often roughly normal to the foliation. The other main crystallographic axes are more dispersed (Fig. 6). Maxima of the poles to (100)_{Pl} or (001)_{Pl} subparallel to the lineation are observed in some cases, but this orientation does not correlate to the textural position of plagioclase (i.e., dispersed in the rock matrix or within olivine- and plagioclase-rich bands) (Fig. 6 and Supplementary Fig. S2).

5.3. Mineral chemistry profiles across peridotite lithologies and pyroxenite layering

In the country peridotites, olivine and pyroxenes do not show any X_{Mg} variability between lherzolite and dunite ($X_{Mg} = 0.89–0.90$, profile BG12; Fig. 7a,b). Clinopyroxenes record higher Ti and Al contents in lherzolite (0.014–0.019 and 0.268–0.336 a.p.f.u., respectively, where a. p.f.u. stands for atom per formula unit) than in dunite (0.008–0.013 and 0.242–0.281 a.p.f.u., respectively) (Fig. 7b,c). Na concentration varies from 0.52 to 0.70 wt% and X_{Cr} [$X_{Cr} = Cr/(Cr + Al)$] values range from 0.06 to 0.12, uncorrelated to the lithology, although the lowest values are typically observed in lherzolite (Supplementary Fig. S3 and Table S2). Orthopyroxenes in lherzolite have slightly higher Al content (0.184–0.269 a.p.f.u.) than those in dunite (0.176–0.212 a.p.f.u.) (Fig. 7b). The X_{Cr} of orthopyroxene varies between 0.05 and 0.09, with the lowest values in the lherzolite (Fig. 7c). Ca content in orthopyroxene does not depend on the lithology with values in the range 0.022–0.034 a.p.f.u. (Supplementary Fig. S3 and Table S2). Spinel has rather homogeneous X_{Mg} values (0.70–0.74). In lherzolite they show Ti content (0.004–0.006 a.p.f.u.) and X_{Cr} values (0.15–0.24) higher than in dunites (Ti = 0.001–0.002 a.p.f.u.; $X_{Cr} = 0.14–0.18$) (Fig. 7c).

The geochemical variation along pyroxenite-peridotite cross sections is illustrated for the profile MC17 (Fig. 8). A similar trend is

observed in the profile BG25 (Supplementary Fig. S4). X_{Mg} (up to 0.91) in olivine, pyroxenes, and spinel is rather homogeneous across the dunite, lherzolite and harzburgite lithologies of the distant domains of the host peridotite (0.88–0.90), similar to what observed in the country peridotites (Fig. 7a–b). On the other hand, minor but systematic decrease of X_{Mg} in olivine and pyroxenes is observed towards the pyroxenite layer, this latter showing markedly lower X_{Mg} values (down to 0.86) (Fig. 8a).

Similar to X_{Mg} , the X_{Cr} in pyroxenes varies as a function of the distance from the pyroxenite, rather than of the peridotite mineralogy (Fig. 8b). Clinopyroxenes show larger variability of X_{Cr} than orthopyroxene, but the trends along the profile are similar. Relatively low X_{Cr} values are observed within the websterite (0.02–0.04), intermediate values dominate in the wall-rock peridotites (0.04–0.08) and the highest values (up to 0.11) are observed in the host peridotites, the latter overlapping with the X_{Cr} of orthopyroxene in the country peridotites (Fig. 7c, 8b). Spinel has the lowest X_{Cr} values in the websterite (0.026–0.04), and the highest values in the host peridotite (up to 0.22); hunter-green spinels from wall-rock peridotites have intermediate X_{Cr} values (0.10–0.13) (Fig. 8b). In profile BG25, the X_{Cr} is inversely correlated to X_{Mg} , with highest X_{Mg} values in spinels of the websterite, which likely reflects differences in the extent of plagioclase-facies re-equilibration compared to other sampling profiles (Supplementary Table S2). In clinopyroxenes, Ti content varies in the range 0.016–0.049 a.p.f.u., with the highest values in the center of websterite layer of profile MC17 (Fig. 8c). Na content in clinopyroxene correlates with neither the lithology, nor the distance from the pyroxenite layer (Fig. 8c). Orthopyroxene shows Ti and Ca contents uncorrelated with lithology with values comprised between 0.003 and 0.011 and 0.020–0.031 a.p.f.u., respectively (Fig. 8c). Spinel has rather low Ti contents along the entire profile (0.002–0.007 a.p.f.u.) (Fig. 8c).

In-situ trace element analyses have been performed on the spinel-facies clinopyroxene porphyroclasts in the dunite layer of profile BG12 and wall-rock and host peridotites of profile MC17 (Table 3). Trace element data have been selected in order to exclude as much as possible the effect of re-equilibration with plagioclase, following the approach used by Borghini et al. (2020). Clinopyroxenes in dunite BG12 display homogeneous REE abundances. Their average composition is compared to the REE concentrations in clinopyroxenes of country peridotites in Fig. 9a. Relative to clinopyroxenes in the country peridotites ($La_N/Sm_N = 0.21$ – 0.35 , $Sm_N/Yb_N = 0.88$ – 1.17 , HREEs $>10\times C1$), the BG12 clinopyroxene shows lower LREE depletion ($La_N/Sm_N = 0.42$) and a negative M-HREE-to-HREE slope ($Sm_N/Yb_N = 1.36$) at lower HREE absolute contents ($<10\times C1$) (Fig. 9a).

Fig. 9b displays the average REE compositions of clinopyroxene porphyroclasts analyzed in the pyroxenite, host and wall-rock peridotites, these latter sampled on both sides of the pyroxenite layer in profile MC17 (see Fig. 8 for location). MC17 data are compared to the compositional field defined by the average REE compositions of clinopyroxenes in the pyroxenites from the same EL mantle sectors and the country peridotites (Fig. 9b). Clinopyroxene from pyroxenite MC17 displays LREE depletion ($La_N/Sm_N = 0.10$), a significant HREE enrichment over the MREE ($Sm_N/Yb_N = 0.69$), and plots within the compositional range defined by the REE spectra of average clinopyroxenes from the other EL pyroxenites (Fig. 9b). However, the trace element abundances of clinopyroxenes from these EL pyroxenites were modified by garnet- to spinel-facies re-equilibration. Most clinopyroxenes inherited the trace element signature of precursor garnet, thus not representing anymore their primary magmatic composition (see detailed explanation in Borghini et al., 2016).

Clinopyroxenes in the host peridotites (samples A1, B1 and B2) are characterized by LREE depletion ($La_N/Sm_N = 0.17$ – 0.21) and flat MREE-HREE (Fig. 9b). In spite of different mineralogy (lherzolite vs. harzburgite), clinopyroxenes in the two wall-rock peridotites (samples A4 and C1) show similar REE patterns. They display lower Sm_N/Nd_N ratios (1.23–1.26) relative to clinopyroxenes in the host and country

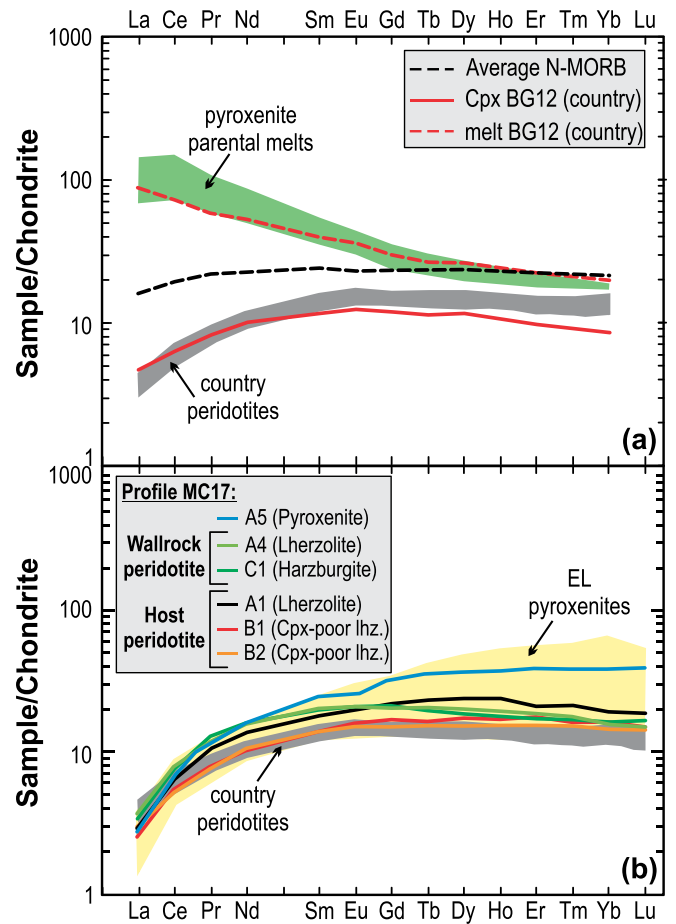


Fig. 9. (a) C1 chondrite-normalized (Anders and Grevesse, 1989) REE pattern of clinopyroxene in the BG12A dunite country peridotite (red solid line) and those of other country peridotites (gray field), the melt in equilibrium with the BG12A clinopyroxene composition (dotted red line), as well as the average N-MORB (dotted black line; Hofmann, 1988) and the estimated pyroxenite parental melts (green field; Borghini et al., 2016). (b) C1 chondrite-normalized (Anders and Grevesse, 1989) REE pattern of clinopyroxene in representative members of the MC17 pyroxenite-peridotite profile (see Fig. 8 for location of thin sections). Note that in sample MC17C1, data were obtained from the wall-rock part of the thin section. The compositional range of country peridotites (gray field) is also plotted for comparison. (For interpretation of the references to color in this figure legend, the reader is referred to the web version of this article.)

peridotites (1.29–1.46), and weak MREE-HREE fractionation ($Sm_N/Yb_N = 1.19$ – 1.28) (Fig. 9b), similar to clinopyroxenes from wall rocks documented in the same outcrops (Borghini et al., 2020).

6. Discussion

6.1. Physico-chemical conditions of melt-rock reactions in the EL mantle

In the studied EL mantle bodies, peridotites exhibit centimeter-scale modal variability, including dunite-lherzolite and dunite-harzburgite-lherzolite sequences, locally containing pyroxenite layers. The pyroxenite-free chemical profile BG12 shows that the observed modal variability (from lherzolite to harzburgite or dunite) is not coupled to any systematic variation of major element mineral chemistry. Indeed, dunites and harzburgites do not display more refractory mineral compositions (such as systematically high X_{Mg} and X_{Cr}) with respect to lherzolites. Across the dunite-lherzolite contact BG12 (see Fig. 2), X_{Mg} and X_{Cr} of all minerals are similar in the two lithologies, as well as Ni in olivine, Ca in olivine and orthopyroxene, and Na contents in clinopyroxene (Fig. 7; Supplementary Fig. S3 and Table S2). Similar

lack of local chemical gradients has been widely documented in dunite-harzburgite-lherzolite sequences from ophiolitic and orogenic peridotite massifs (e.g., Dygert et al., 2016; Kelemen et al., 1995a; Morgan et al., 2008; Suhr et al., 2003; Tommasi et al., 2006). Combined modal lithological variations at rather constant mineral compositions are best explained by reactive percolation of pyroxene-undersaturated melts through the peridotite, inducing pyroxene dissolution and olivine precipitation (Kelemen et al., 1997; Piccardo and Vissers, 2007; Rampone et al., 2004; Rampone et al., 2020). The lack of local variation in mineral chemistry can be explained by either subsequent chemical equilibration at high temperature by diffusion, and/or preceding buffering of the melt composition to that of the host peridotites, particularly in terms of X_{Mg} . In either case, the formation of harzburgite and dunite layers within the EL lherzolites likely resulted from reactive percolation of silica-undersaturated melts.

The pyroxenite-bearing profiles (e.g., BG25 and MC17) also show no systematic variation in X_{Mg} and X_{Cr} within the peridotites, consistent with formation of harzburgite and dunite by reactive porous flow coupled to differential diffusivity/reaction kinetics in the melt, which led to equilibration in Fe—Mg and Cr—Al contents but not in Si, as discussed above (Fig. 8). The major element variability along these profiles is only correlated to the distance from the pyroxenite layer, independently of the modal composition of wall rock and host peridotites (Fig. 8). Variation in modal composition, particularly enrichment in pyroxene, is also observed with decreasing distance to the pyroxenite layers. However, at the tens of cm scale, the variability of the peridotite mode is not symmetric relative to the pyroxenite (Fig. 1c, 8). We interpret these observations as indicating that the percolation of melts, which led to crystallization of pyroxenite layers, postdated the reactive percolation of silica-undersaturated melts that formed the lithological variation in the peridotites. This conclusion is supported by the similarity of REE patterns in the lherzolite and harzburgite wall rocks of profile MC17 (Fig. 9), suggesting that they have been both overprinted by interaction with pyroxenite-derived melts.

Clinopyroxene in dunite distal from pyroxenite layers (BG12A) are quite homogeneous, being not affected by subsolidus plagioclase-facies re-equilibration. They display an average REE composition marked by lower HREE absolute concentrations ($Yb_N = 8.5 \times C1$) and higher LREE/MREE ratio ($La_N/Sm_N = 0.41$) than clinopyroxene in other country peridotites (Fig. 9a). The REE compositions of computed melt in equilibrium with average clinopyroxene in the dunite match those of E-MORB melts inferred to be parental melts of pyroxenites (Borghini et al., 2016) (Fig. 9a). This suggests that despite the different style of melt-rock reaction required for dunite formation and crystallization of pyroxenite layers, the two melts likely had a common source. Moreover, the slight depletion of HREE over the MREE observed in clinopyroxene from BG12 dunite could reflect the combination of chemical disequilibrium of major elements and sluggish diffusion of trace elements (Oliveira et al., 2020).

Variations through time of the volume and composition of reacting melts percolating via porous flow in mantle peridotite have been inferred for pyroxenite-peridotite associations from orogenic massifs (e.g., Frets et al., 2014; Suhr et al., 2003) and mantle xenoliths (e.g. Tommasi et al., 2016). We therefore conclude that the EL mantle domain records a polyphase event of melt percolation. The earlier phase resulted in the formation of depleted Cpx-poor lherzolite – harzburgite – dunite lithologies. This was followed by melt infiltration causing the crystallization of pyroxenites and the chemical modification of host peridotite, in a compositionally heterogeneous mantle domain. The presence of garnet in the primary mineral assemblage inferred for some pyroxenites indicates that melt percolation occurred in the pressure range of 1.5–2.0 GPa (Borghini et al., 2016; Borghini and Fumagalli, 2018). On the other hand, due to significant subsolidus re-equilibration, it is difficult to constrain the thermal conditions of pyroxenite emplacement. Geothermometric estimates on spinel-facies (less exsolved) pyroxene porphyroclasts in the country peridotites provided

minimum equilibrium temperatures of 1000–1050 °C (Borghini et al., 2011; Rampone et al., 1995).

Borghini et al. (2016) inferred that partial melts from a precursor mafic/pyroxenitic component or a mixed pyroxenite-peridotite source are potential candidates for the pyroxenite parental melt. Similar melts have been reproduced experimentally at 1375 °C and 2.5 GPa (Mallik and Dasgupta, 2012). Moreover, Borghini and Fumagalli (2020) showed that melts with similar chemical features could be produced by partial melting of an olivine-free hybrid pyroxenite at 2 GPa and 1300–1350 °C. In order to avoid rapid crystallization, the infiltrated peridotite should not be significantly colder than the liquidus temperature of percolating melts. However, numerical simulation of the chemical modification recorded by the host peridotite near the pyroxenites implies high crystallization rates for the pyroxenite-producing melts and a rather low porosity of the wall-rock peridotite (Borghini et al., 2020). We thus conclude that melt infiltration and pyroxenite emplacement possibly occurred within peridotites at temperatures ranging between 1100 and 1300 °C.

6.2. Deformation of the EL lithospheric mantle

6.2.1. Intracrystalline deformation mechanisms

The porphyroclastic microstructure of the EL peridotites (Figs. 2b–d, 3e–g) characterized by elongation of olivine and orthopyroxene porphyroclasts, undulose extinction and subgrain boundaries perpendicular to the elongation (insets in Figs. 2d, 3k), recrystallization of olivine, and the well-developed CPO of most of the constituent minerals (Figs. 2b–d, 5c–f) point to deformation accommodated by dislocation creep. The alignment of $[100]_{Ol}$ and $[001]_{Opx}$ crystallographic axes subparallel to the stretching lineation indicates coeval deformation of olivine and orthopyroxenes. Such alignment coupled to the orthorhombic and axial- $[100]$ CPO symmetry of olivine, and the orthorhombic CPO of orthopyroxene is consistent with dominant activation of $(Ok1)[100]$ slip systems in olivine and the $(100)[001]$ slip system in orthopyroxene. The dominant activation of the proposed slip systems is corroborated by the $\langle 0vw \rangle$ rotation axes, with dominant contribution of $[001]$ and $[010]$, accommodating low-angle ($2\text{--}12^\circ$) misorientations in olivine and by the dominant $[010]$ rotation axis in orthopyroxene (Supplementary Fig. S2). The CPO of clinopyroxene in the peridotites is more dispersed than that of olivine and orthopyroxene, but the distribution of $(010)_{Cpx}$ subnormal to the plane of the foliation and the relatively strong point-like maximum of $[001]_{Cpx}$ parallel to the stretching lineation (and to $[001]_{Opx}$ and $[100]_{Ol}$ maxima) suggest that the clinopyroxenes accommodated the same solid-state deformation, essentially by dislocation creep, but were probably less deformed, due to their lower volume fraction and higher strength. The observed overall uniform weakening of the clinopyroxene fabric close to the pyroxenite layers compared to distant country peridotites (Fig. 4e) may reflect increased strain partitioning in a liquid phase close to the pyroxenite layers.

In the EL pyroxenites, orthopyroxene mostly occurs at the peridotite-pyroxenite contact. It records weak yet non-random CPO similar to that of matrix orthopyroxene in the peridotite with $[001]_{Opx}$ distributed subparallel to the stretching lineation (Fig. 5a–b vs. c–e). This observation and the dominant rotation axes around $[010]_{Opx}$ accommodating low-angle misorientations (Supplementary Fig. S2) indicate that orthopyroxene at the contact has been deformed by the same mechanisms as in the peridotites, namely $[001]_{Opx}$ dislocation glide. Clinopyroxene, the most abundant phase in the EL pyroxenites, also records a clear CPO (Fig. 5a–b). The observed EL clinopyroxene CPO is similar to that described in experimentally deformed diopside aggregates (Bystricky and Mackwell, 2001; Mauler et al., 2000) and naturally deformed mantle peridotites, pyroxenites and omphacite-bearing eclogites (e.g., Frets et al., 2012; Frets et al., 2014; Hidas et al., 2013; Mauler et al., 2001; Zhang et al., 2006), where the alignment of crystallographic axes is explained by dominant activation of $(1-10)1/2(110)$, $(110)[001]$ and $(100)[001]$ slip systems (e.g., Bascou et al., 2002; van Roermund

and Boland, 1981). The minor obliquity of the maximum distribution of $[001]_{\text{Cpx}}$ axes in the pyroxenites with respect to the foliation in the peridotite and the peridotite–pyroxenite contacts may be explained by simple shear deformation with low finite strains in the pyroxenites (Fig. 5a–b vs. c–f). The similar CPO and deformation mechanisms in the peridotites and the pyroxenite layers suggest that solid-state ductile deformation affected uniformly the peridotite–pyroxenite assemblages. The dominant slip systems proposed to be responsible for the olivine and pyroxene CPO in the EL ophiolites are commonly observed in mantle rocks deformed at high-temperature, spinel- to plagioclase facies conditions in a fluid-poor environment (e.g., Bascou et al., 2002; Frets et al., 2012; Karato and Wu, 1993; Mainprice et al., 2005; Tielke et al., 2019; Tommasi and Vauchez, 2015).

6.2.2. Re-equilibration in plagioclase facies: Static or dynamic?

Olivine in the pyroxenites is a minor phase and has mostly a secondary origin. It was formed together with plagioclase during the spinel-to-plagioclase facies subsolidus phase transformation (Basch et al., 2020; Borghini et al., 2016), following the univariant reaction: clinopyroxene + orthopyroxene + spinel = plagioclase + 2 × olivine (e.g., Rampone et al., 1993 and references therein). In fertile peridotites, secondary olivines were probably formed by the same reaction as in the pyroxenites, but their amount is negligible compared to the rock-forming matrix olivine. This secondary olivine typically has weak CPO (Fig. 5a–b), which is supported by the overall inverse correlation between the modal amount of plagioclase and the fabric strength of olivine along the profiles (cf. Fig. 4a and c). In the pyroxenite layers, the weak correlation of the maximum of $[100]_{\text{Ol}}$ to the stretching lineation (Fig. 5a–b vs. c–f) may indicate that a very small fraction of olivine is either residual and formed part of the host peridotite prior to the pyroxenite emplacement, or inherited the orientation of a deformed spinel-facies precursor phase (e.g., $[001]_{\text{Cpx}}$ or $[001]_{\text{Opx}}$) by topotaxy during the plagioclase phase transformation reaction. A more detailed investigation is hindered by the scarcity of the olivine data in the pyroxenite layers and by the difficulty in discriminating primary and secondary olivine generations in the fertile peridotites. These observations, suggest nevertheless, that the spinel-to-plagioclase facies phase transformation reaction progressed during nearly static conditions, which postdated the deformation event that resulted in the penetrative CPO of major constituent phases in the EL pyroxenites and peridotites.

However, in many EL peridotites and pyroxenites, plagioclase has a weak yet non-random CPO, which challenges this interpretation (Fig. 6). The internal microstructure of plagioclase is not clear due to the fine grain sizes, but the lack of low-angle misorientations and the very weak fabric suggest that the non-random CPO is probably not a result of deformation by dislocation glide. A detailed analysis of the crystallographic orientation of precursor minerals (i.e., clinopyroxene, orthopyroxene and spinel) with respect to that of plagioclase reveals that, within the same texturally controlled assemblage, (100) , (010) and (001) of either clinopyroxene or, rarely, orthopyroxene are distributed subparallel to $(100)_{\text{Pl}}$, $(010)_{\text{Pl}}$ and $(001)_{\text{Pl}}$, respectively (Fig. 10). This suggests that the weak plagioclase CPO is a result of a topotaxial relationship between pyroxenes and plagioclase during the subsolidus transition from the spinel- to plagioclase lherzolite stability field. Considering that these precursor phases have a penetrative CPO that formed during ductile deformation discussed earlier (e.g., $(010)_{\text{Cpx}}$ parallel to the foliation, Fig. 5), plagioclase may have inherited a non-random distribution of its main crystallographic axes, which is aligned with the tectonic foliation and stretching lineation. Weakening of CPO strength during phase transition from parent to product phases of different crystal symmetries is a well-known phenomenon (e.g., austenite to martensitic transformation, Sum and Jonas, 1999), which may explain why the plagioclase CPO is more dispersed than that of its precursor phases.

These observations imply postkinematic formation of secondary olivine and plagioclase at the expense of deformed spinel-facies precursor minerals. Therefore, we propose that the main deformation event

recorded in the EL mantle section occurred in the spinel lherzolite facies at moderate- to high-temperature conditions. This event resulted in the formation of pervasively foliated mantle rocks with penetrative olivine and pyroxene CPO, as well as spinel stretching lineation. By the time the assemblage reached the plagioclase stability field during the exhumation of the massif towards the surface, the deformation of this mantle section had stopped. The phase transformation reaction hence progressed under static conditions producing nearly random CPO of secondary olivine and weak CPO of plagioclase through topotaxial relationship with precursor pyroxenes. Thus, the remaining open question concerns the relative timing between the spinel-facies deformation and the events of melt percolation and melt infiltration that originate the mineralogical variability in peridotite (i.e., dunite and harzburgite) and the pyroxenite emplacement with local peridotite metasomatism, respectively.

6.3. Timing and relationship between melt infiltration and deformation in the EL lithospheric mantle

Detailed analysis of the relationship between pyroxenite layering and the deformation structures of the peridotites (i.e., tectonic foliation and lineation) as well as of the chemical gradients, microstructures and the CPO of the constituent minerals in both peridotites and pyroxenites allows constraining the relative timing of deformation and melt infiltration leading to the pyroxenites emplacement within the EL mantle.

Postkinematic percolation of the pyroxenite-producing melts can be excluded, because it implies near solidus conditions associated with the presence of reactive interstitial melts, which would result in fast annealing of the plastic deformation structures through recovery and static recrystallization processes in the peridotites (e.g., Aradi et al., 2017; Hidas et al., 2016; Liptai et al., 2019; Rampone et al., 2010; Tommasi et al., 2008). Moreover, although melt percolation controlled by the preexisting structure of the peridotites has been proposed to explain small-scale features, for instance, the orientation of mm-scale websterite lenses within harzburgite in the Lherz massif (Le Roux et al., 2008), such anisotropic percolation cannot play a major role when large melt/rock ratios are at play. Thus, the rough parallelism of the pyroxenite layers and the peridotites foliation excludes post-kinematic emplacement of the pyroxenites. The last and major argument against postkinematic reactive melt percolation is that the pyroxenites display microstructures and CPO indicating that they were submitted to the same solid-state deformation as the peridotites (Figs. 2–5).

Was the pyroxenites emplacement thus pre- or synkinematic? The diffuse contacts, at the cm to mm scale, between pyroxenites and peridotites (Fig. 3d; samples BG13A,B and BG25C in Supplementary Fig. S2) favor a synkinematic emplacement. These petrographic features are not compatible with prekinematic formation of the pyroxenite layers and their subsequent tectonic transposition parallel to the foliation, because the large strains needed to produce parallelism would have erased the irregularity of the lithological contacts. Moreover, such large strains would have produced boudinage and intrafolial folds of the more competent pyroxenite layers, similar to veined mantle sections of other orogenic peridotite massifs submitted to high strains under solid-state conditions (Frets et al., 2012, 2014; Henry et al., 2017; Le Roux et al., 2008; Soustelle et al., 2009), and these structures are not observed in the studied EL mantle unit. The preservation of the chemical gradients perpendicular to the layering (Fig. 8, see also chemical profiles in Borghini et al., 2020) further support synkinematic emplacement of the pyroxenites followed by limited solid-state deformation with the same kinematics, which solely produced minor displacement of domains of similar composition parallel to the layering. Moderate solid-state deformation after the crystallization of the pyroxenites is consistent with the higher dispersion of pyroxene CPO in the pyroxenites than in the peridotites (cf. Fig. 5a–b vs. c–f).

Pyroxenite formation in the EL mantle sequence is consistent with melt infiltration and in-situ melt-peridotite reaction as simulated in recent experimental studies (Mallik and Dasgupta, 2012; Wang et al.,

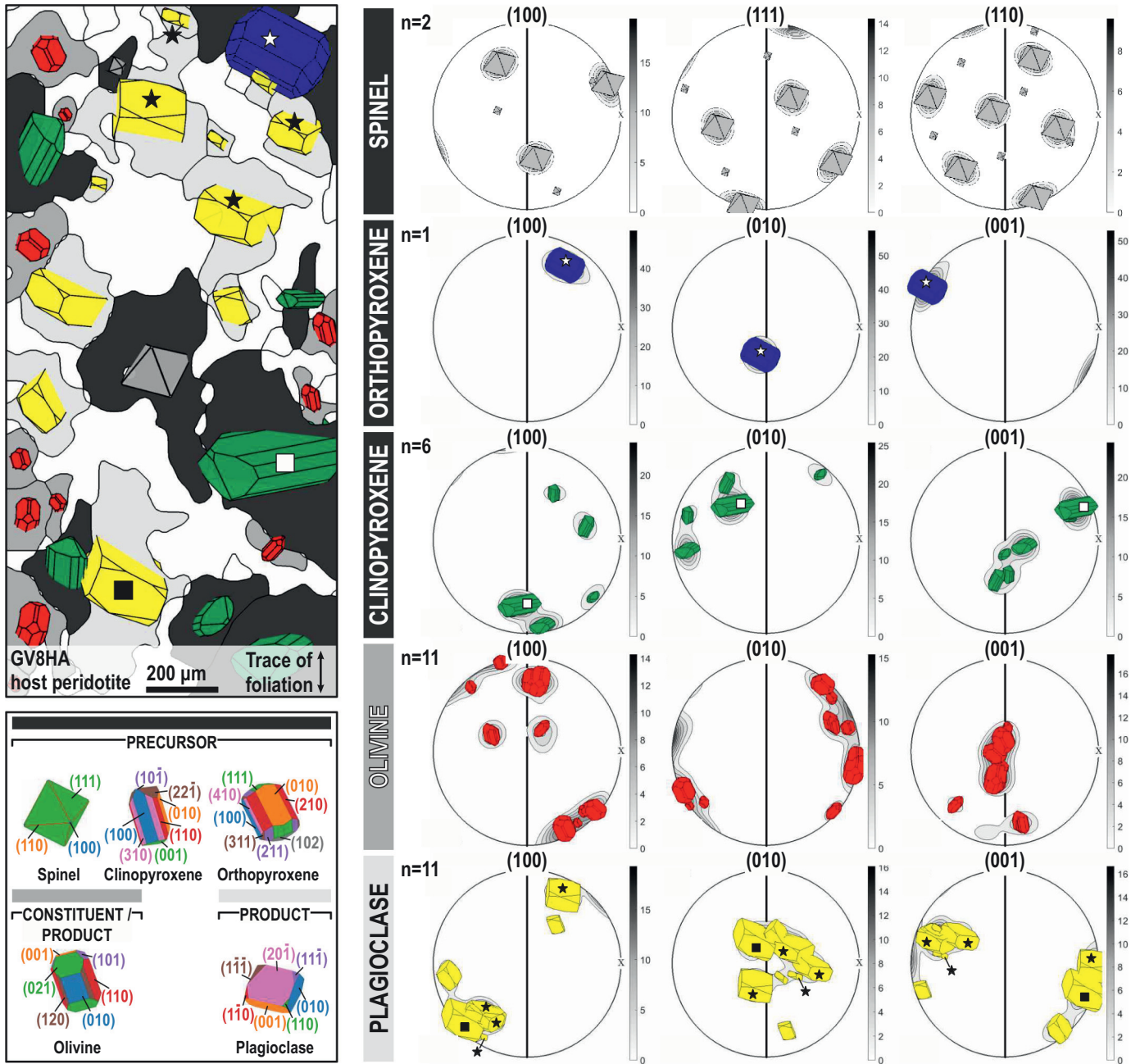


Fig. 10. Crystallographic relationship between plagioclase and precursor pyroxenes in an assemblage that formed during the metamorphic phase transformation reaction from the spinel to plagioclase lherzolite facies upon decompression and cooling of the EL ophiolite to shallow lithospheric mantle depths. The parent-daughter relationship between precursor phases (clinopyroxene or orthopyroxene; white symbols) and product plagioclase (black filled symbols) is indicated for minerals in close textural contact in the map and highlighted in the pole figures. Note that olivine is both a main constituent phase of peridotites and a product of the phase transformation reaction. Pole figures are lower-hemisphere, equal-area stereographic plots using mean orientation of the grains that appear in the selected area with contours at 0.5 multiples of a uniform distribution; n = number of grains. Orientation data is plotted in the sample reference frame, where foliation is vertical (solid line) and lineation is at 0°. Crystal shapes serve as a visual guide to cross-correlate crystals between map and pole figures and their size is proportional to their area in the map. The indices of drawn crystals faces are shown in the legend. The location of the assemblage in the thin section is shown as a white square in Fig. 3f.

2016, 2020). Analysis of chemical gradients in the studied cross sections indicates that, although most of the melt flow was focused in layers parallel or at <20° to the foliation, there was also limited pervasive melt percolation into the peridotite wall rock. This conclusion is also supported by the occurrence of fine-grained anastomosing domains enriched in pyroxenes subparallel to the foliation in the country peridotites (green arrows in Fig. 2b) and their increasing abundance towards the pyroxenite layer (Fig. 3d–g and other members of the GV8 profile in Supplementary Fig. S2). Deformation assisted by small melt fractions may also explain the weaker fabrics of olivine and orthopyroxene in the host and wall rock peridotites compared to those in the country

peridotites (Fig. 4c–d; country vs. wall-rock and host peridotites), since the presence of melts results in part of the deformation being accommodated by diffusional processes. A similar interpretation was proposed to explain the decrease in CPO strength despite macroscopic observations indicating high strain in the Lherz peridotites (Le Roux et al., 2008). Nevertheless, chemical gradients around pyroxenes can also form by partial melting of pristine mafic layers and the in-situ reaction with the host peridotite as described by Sergeev et al. (2014) in pyroxenite-peridotite sequences of Pindos Ophiolites (Northern Greece). However, this model can be discarded in the EL mantle sequence because there are no melting residues associated with

pyroxenites on the field, and a partial melting event would have also reset the deformation features in pyroxenites.

Experimental deformation studies of partially molten olivine aggregates show that, in the presence of melts, olivine CPO symmetry tends to switch from orthorhombic to axial-[010] pattern (Holtzman et al., 2003). Such a switch in olivine CPO symmetry is often cited as an evidence for the presence of melts during deformation of mantle peridotites (e.g., Hidas et al., 2019; Higgie and Tommasi, 2012; Le Roux et al., 2007; Liu et al., 2019; Qi et al., 2018). Nevertheless, the results of Holtzman et al. (2003) suggest that small instantaneous melt fractions (<6% in their experiments) do not result in a switch of olivine CPO. At such low melt fractions, melts are mostly confined at triple junctions and grain boundaries and act as fast diffusion path increasing the contribution of diffusion to the deformation, leading to the decrease in CPO intensity (Hirth and Kohlstedt, 1995a, 1995b; Holtzman et al., 2003). Therefore, the weaker orthorhombic olivine CPO patterns of the EL wall-rock and host peridotites compared to pyroxenite-free country peridotites (Fig. 4c) are consistent with low synkinematic instantaneous melt fractions, which are also inferred for the reaction between tholeiitic melts and peridotite wall rock during the formation of EL pyroxenites (Borghini et al., 2016, 2020).

A similar reasoning may be developed concerning the dunite-forming melt-rock reactions. The lherzolite–harzburgite–dunite lithological boundaries are parallel to the tectonic foliation and, despite

the fact that they are sharper than the pyroxenite–peridotite ones, small-scale irregularities are still preserved (Fig. 2). Although the evidence is less robust and the intensity of the solid-state deformation following the melt–rock reactions is higher, there is an indication for development of the lithological heterogeneity in the country peridotites during the earlier stages of the same deformation event. This further suggests a reduced time-span between the two melt percolation events. These observations corroborate synkinematic melt transport at the base of the EL lithospheric mantle and imply positive feedback of ductile deformation on melt percolation, which led to melt focusing in channels parallel or at low angle (<20°) to the peridotite foliation, that was parallel or at low angle to the shear plane during this deformation.

6.4. Interplay between melt infiltration and deformation: A model for melt intrusion in the deep lithospheric mantle

Many field observations and microstructural studies have documented a strong feedback between melt transport and deformation in mantle rocks in various tectonic settings worldwide (e.g., Brown and Solar, 1998; Frets et al., 2014; Hidas et al., 2019; Higgie and Tommasi, 2012, 2014; Kelemen and Dick, 1995; Le Roux et al., 2008; Rosenberg, 2004; Tommasi et al., 1994; Tommasi et al., 2016). The observations in the EL pyroxenite-bearing veined mantle are consistent with these

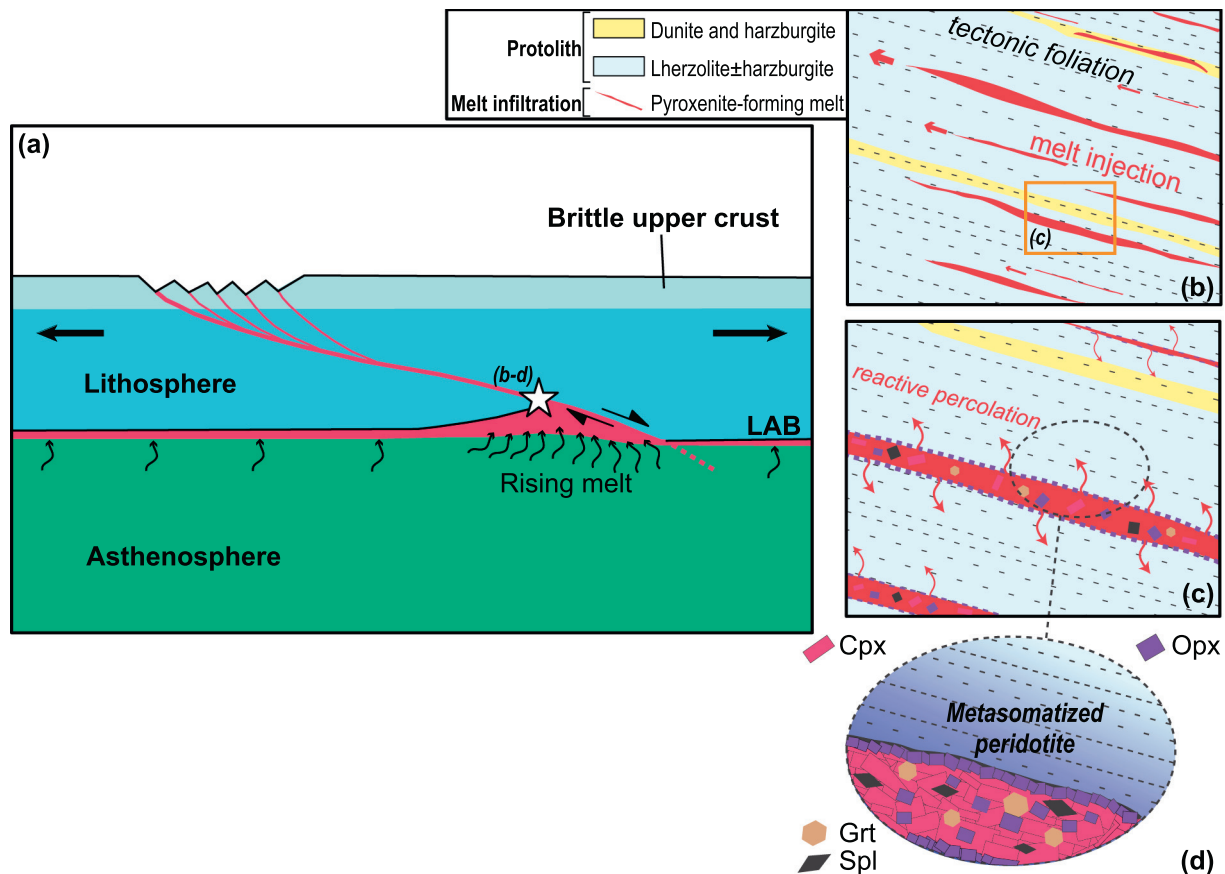


Fig. 11. Conceptual model for the pyroxenite emplacement and formation of veined mantle via stress-driven melt infiltration at the lithosphere–asthenosphere boundary (LAB). (a) Melt accumulation at the LAB as described by Sakamaki et al. (2013). Lithosphere extension enhances melt production and accumulation, in turn, leading to rheological weakening and shear deformation. (b) Melt injection mainly along tectonic foliation (dotted lines), which was generated during coeval ductile deformation (red arrows indicate the direction of melt infiltration). Yellow-shaded areas indicate pre-existing compositional heterogeneities in the peridotites (i.e., dunite and harzburgite) that probably formed during the earlier stages of the same deformation event. Note that pyroxenite-forming melts may percolate along both compositional and rheological heterogeneities (i.e., melt percolation is parallel to dotted lines and yellow patches), but refractory peridotites are not always associated with pyroxenite melt percolation (i.e., there are yellow patches without melt percolation). (c) Reactive percolation of melts from the melt-rich veins into the adjacent peridotite coeval to pyroxenite crystallization; dashed purple lines indicate development of a reaction zone at the pyroxenite–peridotite contact. (d) Schematic sketch of the resulting veined mantle as documented in the studied units of the EL ophiolites. Cpx: clinopyroxene; Grt: garnet; Opx: orthopyroxene; Sp: spinel. Note that the re-equilibration in the Seiland subfacies and in the plagioclase lherzolite facies is not addressed in the figure. (For interpretation of the references to color in this figure legend, the reader is referred to the web version of this article.)

previous results and points to the role of deformation in melt transport and melt intrusion into peridotite at the lithosphere-asthenosphere boundary (LAB), leading to the pyroxenite emplacement at great depths. Borghini et al. (2016) documented that pyroxenites formed in the Late Ordovician-Silurian, and suggested that the parental melts are related to mantle upwelling and melting during lithosphere extension and opening of the Paleo-Tethys oceanic basin (von Raumer et al., 2013 and references therein).

In Fig. 11, we present a conceptual model for the Paleozoic tectonic and petrological evolution of the EL mantle and the synkinematic emplacement of pyroxenite veins. Mantle partial melting and melts accumulation are triggered at the LAB through decompression in response to lithospheric extension (Fig. 11a–b). Melt stagnation at the LAB might have produced rheological weakening, enhanced shear deformation, and formation of sub-horizontal melt-rich layers (Bruhn et al., 2000; Holtzman et al., 2003; Zimmerman et al., 1999). In a scenario of extensional dynamics, melt segregation in layers parallel to the shear plane would further enhance melt transport along detachment faults (e.g., Higgie and Tommasi, 2014; Kaczmarek and Müntener, 2008; Kaczmarek and Tommasi, 2011; Soustelle et al., 2009).

In the EL mantle domain, deformation triggered by lithosphere extension likely resulted in the development of pervasive tectonic foliation in peridotites (Fig. 11a–b). Melt accumulation at the LAB combined with deformation potentially drove the pooled melts along the foliation planes, leading to the infiltration of the overlying lithosphere (Fig. 11b). Our results indicate that the infiltrating melts have been channeled along the shear plane (Fig. 11c). In these channels, the melt/peridotite ratio is high and the melt composition controls the chemistry of the pyroxenites, hence the chemical signature of the original infiltrating melts is best recorded by the composition of the largest pyroxenite layers, as documented by the correlation between pyroxenite layer thickness and their chemistry (e.g. bulk X_{Mg} and NiO content) in the Ronda massif (Bodinier et al., 2008; Fabries et al., 2001) and in the External Liguride ophiolites as well (Borghini et al., 2016). Pervasive percolation of melts from these channels into the first centimeters of the host peridotites (Fig. 11c–d) led to development of metasomatized aureoles that acquired an *E*-MORB-like geochemical signature (Borghini et al., 2020).

The melt intrusion into peridotites also changed the deformation processes, favoring diffusion and probably leading to local transient weakening of these layers. The distribution of melts was therefore controlled by deformation that, in turn, controlled not only the changes in chemical composition, but the rheology of the mantle rocks as well. We thus propose that the interplay between melt infiltration and deformation represents an efficient mechanism for both mantle refertilization and formation of mantle heterogeneities at deep lithospheric conditions.

7. Concluding summary

We present geochemical and microstructural data to support a poly-phase event of melt percolation likely originating from a common source in the External Liguride mantle domain: i) an earlier stage leading to formation of reactive harzburgite and dunite lithotypes associated to predominant lherzolites and ii) a subsequent stage producing pyroxenite layering. Microstructural data show that deformation leading to development of a pervasive foliation and lineation in all lithologies occurred at spinel lherzolite-facies conditions and was synkinematic to pyroxenite emplacement. Evidence for synkinematic melt percolation includes: (i) the parallelism between lithological contacts and the tectonic foliation coupled to irregularities of lithological contacts, and the absence of boudinage or intrafolial folds, ruling out tectonic transposition, (ii) preserved geochemical gradient across pyroxenite-peridotite boundaries, and (iii) the well-developed CPO of spinel-facies silicate minerals with decreasing fabric strength in the peridotites close to the pyroxenites compared to distal peridotites. These results point to melt

focusing along or at low angle to the shear plane, indicating a strong interplay between melt infiltration and deformation in the formation of pyroxenite layering in deep sections of the lithospheric mantle.

Supplementary data to this article can be found online at <https://doi.org/10.1016/j.lithos.2020.105855>.

Declaration of Competing Interest

The authors declare that they have no known competing financial interests or personal relationships that could have appeared to influence the work reported in this paper.

Acknowledgements

L. Negretti and A. Risplendente are thanked for technical assistance with the EDS and WDS analyses. We are grateful to D. Mainprice (Géosciences Montpellier, France) for providing scripts and help in MTEX, and to L.E. Aradi (Lithosphere Fluid Research Lab, Budapest) for contributing to an earlier version of the EBSD database. We thank C.J. Garrido for fruitful discussions. We appreciate the constructive comments by Romain Tilhac and an anonymous reviewer, as well as the editorial handling by Marco Scambelluri.

This work was financially supported by the Italian Ministry of Education, University and Research (MIUR, Italy) [grant no. PRIN-2015C5LN35] "Melt rock reaction and melt migration in the MORB mantle through combined natural and experimental studies. Research leading to these results was also funded by K.H.'s European Union 7th Framework Programme Marie Curie postdoctoral grant [grant no. PIF-GA-2012-327226]. K.H. further acknowledges funding by the Ministerio de Economía y Competitividad (Spain) [grant no. FPD1-2013-16253] and the Agencia Estatal de Investigación (Spain) [grant no. CGL2016-81085-R]. Fellowships, research and infrastructure grants have been co-funded by the European Social Fund (ESF) and the European Regional Development Fund (ERFD) of the European Commission.

References

- Anders, E., Grevesse, N., 1989. Abundances of the elements: Meteoritic and solar. *Geochim. Cosmochim. Acta* 53, 197–214.
- Aradi, L.E., Hidas, K., Kovács, I.J., Tommasi, A., Klébesz, R., Garrido, C.J., Szabó, C., 2017. Fluid-enhanced annealing in the subcontinental lithospheric mantle beneath the westernmost margin of the Carpathian-Pannonian extensional basin system. *Tectonics* 36, 2987–3011.
- Bachmann, F., Hielscher, R., Schaeben, H., 2010. Texture analysis with MTEX - free and open source software toolbox. *Solid State Phenom.* 160, 63–68.
- Bachmann, F., Hielscher, R., Schaeben, H., 2011. Grain detection from 2d and 3d EBSD data - Specification of the MTEX algorithm. *Ultramicroscopy* 111, 1720–1733.
- Basch, V., Borghini, G., Fumagalli, P., Rampone, E., Ferrando, C., Gandolfo, A., 2020. Plagioclase-facies thermobarometric evolution of the External Liguride pyroxenite-bearing mantle (Suvero, Italy). *Ophioliti* 45, 11.
- Bascou, J., Tommasi, A., Mainprice, D., 2002. Plastic deformation and development of clinopyroxene lattice preferred orientations in eclogites. *J. Struct. Geol.* 24, 1357–1368.
- Bill, M., O'Dogherty, L., Guex, J., Baumgartner, P.O., Masson, H., 2001. Radiolarite ages in Alpine-Mediterranean ophiolites: Constraints on the oceanic spreading and the Tethys-Atlantic connection. *GSA Bull.* 113, 129–143.
- Bodinier, J.L., Godard, M., 2014. 3.4 - Orogenic, ophiolitic, and abyssal peridotites. In: Turekian, H.D.H.K. (Ed.), *Treatise on Geochemistry*, Second edition Elsevier, Oxford, pp. 103–167.
- Bodinier, J.L., Garrido, C.J., Chanefo, I., Bruguier, O., Gervilla, F., 2008. Origin of pyroxenite-peridotite veined mantle by refertilization reactions: evidence from the Ronda peridotite (Southern Spain). *J. Petrol.* 49, 999–1025.
- Borghini, G., Fumagalli, P., 2018. Subsolvus phase relations in a mantle pyroxenite: an experimental study from 0.7 to 1.5 GPa. *Eur. J. Mineral.* 30, 333–348.
- Borghini, G., Fumagalli, P., 2020. Melting relations of anhydrous olivine-free pyroxenite Px1 at 2 GPa. *Eur. J. Mineral.* 32, 251–264.
- Borghini, G., Fumagalli, P., Rampone, E., 2011. The geobarometric significance of plagioclase in mantle peridotites: a link between nature and experiments. *Lithos* 126, 42–53.
- Borghini, G., Rampone, E., Zanetti, A., Class, C., Cipriani, A., Hofmann, A.W., Goldstein, S.L., 2013. Meter-scale Nd isotopic heterogeneity in pyroxenite-bearing Ligurian peridotites encompasses global-scale upper mantle variability. *Geology* 41, 1055–1058.

- Borghini, G., Rampone, E., Zanetti, A., Class, C., Cipriani, A., Hofmann, A.W., Goldstein, S.L., 2016. Pyroxenite layers in the Northern Apennines' upper mantle (Italy) – generation by pyroxenite melting and melt infiltration. *J. Petrol.* 57, 625–653.
- Borghini, G., Rampone, E., Zanetti, A., Class, C., Fumagalli, P., Godard, M., 2020. Ligurian pyroxenite-peridotite sequences (Italy) and the role of melt-rock reaction in creating enriched-MORB mantle sources. *Chem. Geol.* 532, 119252.
- Brown, M., Solar, G.S., 1998. Shear-zone systems and melts: feedback relations and self-organization in orogenic belts. *J. Struct. Geol.* 20, 211–227.
- Bruhn, D., Groebner, N., Kohlstedt, D.L., 2000. An interconnected network of core-forming melts produced by shear deformation. *Nature* 403, 883–886.
- Brunelli, D., Cipriani, A., Bonatti, E., 2018. Thermal effects of pyroxenites on mantle melting below mid-ocean ridges. *Nat. Geosci.* 11, 520–525.
- Bystricky, M., Mackwell, S., 2001. Creep of dry clinopyroxene aggregates. *J. Geophys. Res.* 106, 13443–13413, 13454.
- Cao, Y., Jung, H., Song, S., Park, M., Jung, S., Lee, J., 2015. Plastic deformation and seismic properties in fore-arc mantles: a petrofabric analysis of the Yushigou harzburgites, North Qilian suture zone, NW China. *J. Petrol.* 56, 1897–1944.
- Donnelly, K.E., Goldstein, S.L., Langmuir, C.H., Spiegelman, M., 2004. Origin of enriched ocean ridge basalts and implications for mantle dynamics. *Earth Planet. Sci. Lett.* 226, 347–366.
- Dyger, N., Liang, Y., Kelemen, P.B., 2016. Formation of plagioclase lherzolite and associated dunite-harzburgite-lherzolite sequences by multiple episodes of melt percolation and melt-rock reaction: an example from the Trinity Ophiolite, California, USA. *J. Petrol.* 57, 815–838.
- Fabries, J., Lorand, J.P., Guiraud, M., 2001. Petrogenesis of the amphibole-rich veins from the Lherz orogenic lherzolite massif (Eastern Pyrenees, France): a case study for the origin of orthopyroxene-bearing amphibole pyroxenites in the lithospheric mantle. *Contrib. Mineral. Petrol.* 140, 383–403.
- Fernández-Roig, M., Galán, G., Mariani, E., 2017. Deformation and seismic anisotropy of the subcontinental lithospheric mantle in NE Spain: EBSD data on xenoliths from the Catalan Volcanic Zone. *Tectonophysics* 698, 16–37.
- Frets, E., Tommasi, A., Garrido, C.J., Padrón-Navarta, J.A., Amri, I., Targuisti, K., 2012. Deformation processes and rheology of pyroxenites under lithospheric mantle conditions. *J. Struct. Geol.* 39, 138–157.
- Frets, E.C., Tommasi, A., Garrido, C.J., Vauchez, A., Mainprice, D., Targuisti, K., Amri, I., 2014. The Beni Bousera Peridotite (Cif Belt, Morocco): an Oblique-slip Low-angle Shear Zone Thinning the Subcontinental Mantle Lithosphere. *J. Petrol.* 55, 283–313.
- Fumagalli, P., Borghini, G., Rampone, E., Poli, S., 2017. Experimental calibration of Forsterite–Anorthite–Ca–Tschermark–Enstatite (FACE) geobarometer for mantle peridotites. *Contrib. Mineral. Petrol.* 172, 38.
- Garrido, C.J., Bodinier, J.L., 1999. Diversity of mafic rocks in the Ronda peridotite: evidence for pervasive melt-rock reaction during heating of subcontinental lithosphere by upwelling asthenosphere. *J. Petrol.* 40, 729–754.
- Henry, H., Tilhac, R., Griffin, W.L., O'Reilly, S.Y., Satsukawa, T., Kaczmarek, M.-A., Grégoire, M., Ceuleneer, G., 2017. Deformation of mantle pyroxenites provides clues to geodynamic processes in subduction zones: Case study of the Cabo Ortegal complex, Spain. *Earth Planet. Sci. Lett.* 472, 174–185.
- Hidas, K., Garrido, C.J., Tommasi, A., Padrón-Navarta, J.A., Thielmann, M., Konc, Z., Frets, E., Marchesi, C., 2013. Strain localization in pyroxenite by reaction-enhanced softening in the shallow subcontinental lithospheric mantle. *J. Petrol.* 54, 1997–2031.
- Hidas, K., Tommasi, A., Garrido, C.J., Padrón-Navarta, J.A., Mainprice, D., Vauchez, A., Barou, F., Marchesi, C., 2016. Fluid-assisted strain localization in the shallow subcontinental lithospheric mantle. *Lithos* 262, 636–650.
- Hidas, K., Garrido, C.J., Booth-Rea, G., Marchesi, C., Bodinier, J.L., Dautria, J.M., Louni-Hacini, A., Azzouni-Sekkal, A., 2019. Lithosphere tearing along STEP faults and synkinematic formation of lherzolite and wehrlite in the shallow subcontinental mantle. *Solid Earth* 10, 1099–1121.
- Hielscher, R., Schaeben, H., 2008. A novel pole figure inversion method: specification of the MTEX algorithm. *J. Appl. Crystallogr.* 41, 1024–1037.
- Higgie, K., Tommasi, A., 2012. Feedbacks between deformation and melt distribution in the crust-mantle transition zone of the Oman ophiolite. *Earth Planet. Sci. Lett.* 359, 61–72.
- Higgie, K., Tommasi, A., 2014. Deformation in a partially molten mantle: Constraints from plagioclase lherzolites from Lanzo, western Alps. *Tectonophysics* 615, 167–181.
- Hirschmann, M.M., Stolper, E.M., 1996. A possible role for garnet pyroxenite in the origin of the “garnet signature” in MORB. *Contrib. Mineral. Petrol.* 124, 185–208.
- Hirth, G., Kohlstedt, D.L., 1995a. Experimental constraints on the dynamics of the partially molten upper-mantle - Deformation in the diffusion creep regime. *J. Geophys. Res.* Solid Earth 100, 1981–2001.
- Hirth, G., Kohlstedt, D.L., 1995b. Experimental constraints on the dynamics of the partially molten upper-mantle - Deformation in the dislocation creep regime. *J. Geophys. Res.* Solid Earth 100, 15441–15449.
- Hofmann, A.W., 1988. Chemical differentiation of the Earth - the relationship between mantle, continental crust, and oceanic crust. *Earth Planet. Sci. Lett.* 90, 297–314.
- Holtzman, B.K., Kohlstedt, D.L., Zimmerman, M.E., Heidelbach, F., Hiraga, T., Hustofo, J., 2003. Melt segregation and strain partitioning: Implications for seismic anisotropy and mantle flow. *Science* 301, 1227–1230.
- Kaczmarek, M.-A., Müntener, O., 2008. Juxtaposition of melt impregnation and high-temperature shear zones in the upper mantle; Field and petrological constraints from the Lanzo Peridotite (Northern Italy). *J. Petrol.* 49, 2187–2220.
- Kaczmarek, M.-A., Tommasi, A., 2011. Anatomy of an extensional shear zone in the mantle, Lanzo massif, Italy. *Geochem. Geophys. Geosyst.* 12, Q0AG06.
- Kaczmarek, M.-A., Jonda, L., Davies, H.L., 2015. Evidence of melting, melt percolation and deformation in a supra-subduction zone (Marum ophiolite complex, Papua New Guinea). *Contrib. Mineral. Petrol.* 170, 19.
- Karato, S.-I., Wu, P., 1993. Rheology of the upper mantle: a synthesis. *Science* 260, 771–778.
- Katz, R.F., Weatherley, S.M., 2012. Consequences of mantle heterogeneity for melt extraction at mid-ocean ridges. *Earth Planet. Sci. Lett.* 335–336, 226–237.
- Kelemen, P.B., Dick, H.J.B., 1995. Focused melt flow and localized deformation in the upper mantle - Juxtaposition of replacive dunite and ductile shear zones in the Josephine Peridotite, SW Oregon. *J. Geophys. Res.* Solid Earth 100, 423–438.
- Kelemen, P.B., Shimizu, N., Salters, V.J.M., 1995a. Extraction of Mid-Ocean-Ridge Basalt from the Upwelling Mantle by Focused Flow of Melt in Dunite Channels. *Nature* 375, 747–753.
- Kelemen, P.B., Whitehead, J.A., Aharonov, E., Jordahl, K.A., 1995b. Experiments on flow focusing in soluble porous-media, with applications to melt extraction from the mantle. *J. Geophys. Res.* Solid Earth 100, 475–496.
- Kelemen, P.B., Hirth, G., Shimizu, N., Spiegelman, M., Dick, H.J., 1997. A review of melt migration processes in the adiabatically upwelling mantle beneath oceanic spreading ridges. *Philos. Trans. R. Soc. A Math. Phys. Eng. Sci.* 355, 283–318.
- Kogiso, T., Hirschmann, M.M., Pertermann, M., 2004. High-pressure Partial Melting of Mafic Lithologies in the Mantle. *J. Petrol.* 45, 2407–2422.
- Lambart, S., Laporte, D., Provost, A., Schiano, P., 2012. Fate of pyroxenite-derived melts in the peridotitic mantle: thermodynamic and experimental constraints. *J. Petrol.* 53, 451–476.
- Lambart, S., Laporte, D., Schiano, P., 2013. Markers of the pyroxenite contribution in the major-element compositions of oceanic basalts: Review of the experimental constraints. *Lithos* 160, 14–36.
- Lambart, S., Baker, M.B., Stolper, E.M., 2016. The role of pyroxenite in basalt genesis: Melt-PX, a melting parameterization for mantle pyroxenites between 0.9 and 5 GPa. *J. Geophys. Res.* Solid Earth 121, 5708–5735.
- Le Roux, V., 2008. Melt-Rock Interactions and Melt-Assisted Deformation in the Lherz Peridotite, with Implications for the Structural, Chemical and Isotopic Evolution of the Lithospheric Mantle, Géosciences Montpellier. Université Montpellier II. Université Montpellier II, Montpellier, France, p. 158.
- Le Roux, V., Bodinier, J.L., Tommasi, A., Alard, O., Dautria, J.M., Vauchez, A., Riches, A.J.V., 2007. The Lherz spinel lherzolite: Refertilized rather than pristine mantle. *Earth Planet. Sci. Lett.* 259, 599–612.
- Le Roux, V., Tommasi, A., Vauchez, A., 2008. Feedback between melt percolation and deformation in an exhumed lithosphere-asthenosphere boundary. *Earth Planet. Sci. Lett.* 274, 401–413.
- Lemoine, M., Trümpy, R., 1987. Pre-oceanic rifting in the Alps. *Tectonophysics* 133, 305–320.
- Liptai, N., Hidas, K., Tommasi, A., Patkó, L., Kovács, I.J., Griffin, W.L., O'Reilly, S.Y., Pearson, N.J., Szabó, C., 2019. Lateral and vertical heterogeneity in the lithospheric mantle at the northern margin of the Pannonian Basin reconstructed from peridotite xenolith microstructures. *J. Geophys. Res.* Solid Earth 124, 6315–6336.
- Liu, S., Tommasi, A., Vauchez, A., Mazzucchelli, M., 2019. Deformation, annealing, melt-rock interaction, and seismic properties of an old domain of the Equatorial Atlantic lithospheric mantle. *Tectonics* 38, 1164–1188.
- Mainprice, D., Tommasi, A., Couvy, H., Cordier, P., Frost, D.J., 2005. Pressure sensitivity of olivine slip systems and seismic anisotropy of Earth's upper mantle. *Nature* 433, 731–733.
- Mallik, A., Dasgupta, R., 2012. Reaction between MORB-eclogite derived melts and fertile peridotite and generation of ocean island basalts. *Earth Planet. Sci. Lett.* 329–330, 97–108.
- Manatschal, G., Müntener, O., 2009. A type sequence across an ancient magma-poor ocean-continent transition: the example of the western Alpine Tethys ophiolites. *Tectonophysics* 473, 4–19.
- Marchesi, C., Garrido, C.J., Bosch, D., Bodinier, J.-L., Gervilla, F., Hidas, K., 2013. Mantle refertilization by melts of crustal-derived garnet pyroxenite: evidence from the Ronda peridotite massif, southern Spain. *Earth Planet. Sci. Lett.* 362, 66–75.
- Marroni, M., Pandolfi, L., 2007. The architecture of an incipient oceanic basin: a tentative reconstruction of the Jurassic Liguria-Piemonte basin along the Northern Apennines-Alpine Corsica transect. *Int. J. Earth Sci.* 96, 1059–1078.
- Mauler, A., Bystricky, M., Kunze, K., Mackwell, S., 2000. Microstructures and lattice preferred orientations in experimentally deformed clinopyroxene aggregates. *J. Struct. Geol.* 22, 1633–1648.
- Mauler, A., Godard, G., Kunze, K., 2001. Crystallographic fabrics of omphacite, rutile and quartz in Vendée eclogites (Armorican Massif, France). Consequences for deformation mechanisms and regimes. *Tectonophysics* 342, 81–112.
- Montanini, A., Harlov, D., 2006. Petrology and mineralogy of granulite-facies mafic xenoliths (Sardinia, Italy): evidence for KCl metasomatism in the lower crust. *Lithos* 92, 588–608.
- Montanini, A., Tribuzio, R., 2015. Evolution of recycled crust within the mantle: Constraints from the garnet pyroxenites of the External Ligurian ophiolites (northern Apennines, Italy). *Geology* 43, 911–914.
- Montanini, A., Tribuzio, R., Anczkiewicz, R., 2006. Exhumation history of a garnet pyroxenite-bearing mantle section from a continent-ocean transition (Northern Apennine ophiolites, Italy). *J. Petrol.* 47, 1943–1971.
- Montanini, A., Tribuzio, R., Vernia, L., 2008. Petrogenesis of basalts and gabbros from an ancient continent-ocean transition (External Liguride ophiolites, Northern Italy). *Lithos* 101, 453–479.
- Montanini, A., Tribuzio, R., Thirlwall, M., 2012. Garnet clinopyroxenite layers from the mantle sequences of the Northern Apennine ophiolites (Italy): evidence for recycling of crustal material. *Earth Planet. Sci. Lett.* 351–352, 171–181.
- Morgan, Z., Liang, Y., Kelemen, P., 2008. Significance of the concentration gradients associated with dunite bodies in the Josephine and Trinity ophiolites. *Geochem. Geophys. Geosyst.* 9, Q07025.

- Müntener, O., Piccardo, G.B., 2003. Melt migration in ophiolitic peridotites: the message from Alpine-Apennine peridotites and implications for embryonic ocean basins. *Geol. Soc. Lond. Spec. Publ.* 218, 69–89.
- Müntener, O., Pette, T., Desmurs, L., Meier, M., Schaltegger, U., 2004. Refertilization of mantle peridotite in embryonic ocean basins: trace element and Nd isotopic evidence and implications for crust–mantle relationships. *Earth Planet. Sci. Lett.* 221, 293–308.
- Oliveira, B., Afonso, J.C., Tilhac, R., 2020. A disequilibrium reactive transport model for mantle magmatism. *J. Petrol.* ega067. <https://doi.org/10.1093/ptrology/egaa067>.
- Phipps Morgan, J., 2001. Thermodynamics of pressure release melting of a veined plum pudding mantle. *Geochim. Geophys. Geosyst.* 2 2000GC000049.
- Picazo, S., Müntener, O., Manatschal, G., Bauville, A., Karner, G., Johnson, C., 2016. Mapping the nature of mantle domains in Western and Central Europe based on clinopyroxene and spinel chemistry: evidence for mantle modification during an extensional cycle. *Lithos* 266–267, 233–263.
- Piccardo, G.B., Vissers, R.L.M., 2007. The pre-oceanic evolution of the Erro-Tobbio peridotite (Voltri Massif, Ligurian Alps, Italy). *J. Geodyn.* 43, 417–449.
- Piccardo, G.B., Müntener, O., Zanetti, A., Pette, T., 2004. Ophiolitic peridotites of the Alpine-Apennine system: mantle processes and geodynamic relevance. *Int. Geol. Rev.* 46, 1119–1159.
- Puziewicz, J., Matusiak-Malek, M., Ntaflou, T., Grégoire, M., Kaczmarek, M.-A., Aulbach, S., Ziobro, M., Kukuła, A., 2020. Three major types of subcontinental lithospheric mantle beneath the Variscan orogen in Europe. *Lithos* 105467.
- Qi, C., Hansen, L.N., Wallis, D., Holtzman, B.K., Kohlstedt, D.L., 2018. Crystallographic Preferred Orientation of olivine in sheared partially molten rocks: the source of the “A-C switch”. *Geochim. Geophys. Geosyst.* 19, 316–336.
- Rampone, E., Piccardo, G.B., Vannucci, R., Bottazzi, P., Ottolini, L., 1993. Subsolidus reactions monitored by trace-element partitioning - the spinel-facies to plagioclase-facies transition in mantle peridotites. *Contrib. Mineral. Petrol.* 115, 1–17.
- Rampone, E., Hofmann, A.W., Piccardo, G.B., Vannucci, R., Bottazzi, P., Ottolini, L., 1995. Petrology, mineral and isotope geochemistry of the External Liguride Peridotites (Northern Apennines, Italy). *J. Petrol.* 36, 81–105.
- Rampone, E., Piccardo, G.B., Vannucci, R., Bottazzi, P., 1997. Chemistry and origin of trapped melts in ophiolitic peridotites. *Geochim. Cosmochim. Acta* 61, 4557–4569.
- Rampone, E., Piccardo, G.B., Dilek, Y., Moores, E.M., Elthon, D., Nicolas, A., 2000. The ophiolite-oceanic lithosphere analogue: New insights from the Northern Apennines (Italy). *Ophiolites and oceanic crust: new insights from field studies and the Ocean Drilling Program. Geological Society of America* p. 0.
- Rampone, E., Romairone, A., Hofmann, A.W., 2004. Contrasting bulk and mineral chemistry in depleted mantle peridotites: evidence for reactive porous flow. *Earth Planet. Sci. Lett.* 218, 491–506.
- Rampone, E., Piccardo, G.B., Hofmann, A.W., 2008. Multi-stage melt–rock interaction in the Mt. Maggiore (Corsica, France) ophiolitic peridotites: microstructural and geochemical evidence. *Contrib. Mineral. Petrol.* 156, 453–475.
- Rampone, E., Vissers, R.L.M., Poggio, M., Scambelluri, M., Zanetti, A., 2010. Melt migration and intrusion during exhumation of the Alboran lithosphere: the Tallante mantle xenolith record (Betic Cordillera, SE Spain). *J. Petrol.* 51, 295–325.
- Rampone, E., Borghini, G., Basch, V., 2020. Melt migration and melt–rock reaction in the Alpine-Apennine peridotites: Insights on mantle dynamics in extending lithosphere. *Geosci. Front.* 11, 151–166.
- Rosenberg, C.L., 2004. Shear zones and magma ascent: A model based on a review of the Tertiary magmatism in the Alps. *Tectonics* 23.
- Rosenthal, A., Yaxley, G.M., Green, D.H., Hermann, J., Kovacs, I., Spandler, C., 2014. Continuous eclogite melting and variable refertilization in upwelling heterogeneous mantle. *Sci. Rep.* 4, 6099.
- Sakamaki, T., Suzuki, A., Ohtani, E., Terasaki, H., Urakawa, S., Katayama, Y., Funakoshi, K.-I., Wang, Y., Hernlund, J.W., Ballmer, M.D., 2013. Ponded melt at the boundary between the lithosphere and asthenosphere. *Nat. Geosci.* 6, 1041–1044.
- Salters, V.J.M., Dick, H.J.B., 2002. Mineralogy of the mid-ocean-ridge basalt source from neodymium isotopic composition of abyssal peridotites. *Nature* 418, 68–72.
- Sanfilippo, A., Tribuzio, R., 2011. Melt transport and deformation history in a nonvolcanic ophiolitic section, northern Apennines, Italy: Implications for crustal accretion at slow spreading settings. *Geochim. Geophys. Geosyst.* 12.
- Sergeev, D.S., Dijkstra, A.H., Meisel, T., Brüggemann, G., Sergeev, S.A., 2014. Traces of ancient mafic layers in the Tethys oceanic mantle. *Earth Planet. Sci. Lett.* 389, 155–166.
- Shorttle, O., MacLennan, J., 2011. Compositional trends of Icelandic basalts: Implications for short-length scale lithological heterogeneity in mantle plumes. *Geochim. Geophys. Geosyst.* 12, Q11008.
- Skemer, P., Katayama, I., Jiang, Z., Karato, S.-I., 2005. The misorientation index: Development of a new method for calculating the strength of lattice-preferred orientation. *Tectonophysics* 411, 157–167.
- Soustelle, V., Tommasi, A., Bodinier, J.L., Garrido, C.J., Vauchez, A., 2009. Deformation and reactive melt transport in the mantle lithosphere above a large-scale partial melting domain: the Ronda Peridotite Massif, southern Spain. *J. Petrol.* 50, 1235–1266.
- Suhr, G., Hellebrand, E., Snow, J.E., Seck, H.A., Hofmann, A.W., 2003. Significance of large, refractory dunite bodies in the upper mantle of the Bay of Islands Ophiolite. *Geochim. Geophys. Geosyst.* 4, 8605.
- Sum, M., Jonas, J.J., 1999. A dislocation reaction model for variant selection during the austenite-to-martensite transformation. *Text. Microstruct.* 31, 187–215.
- Tielke, J., Mecklenburgh, J., Mariani, E., Wheeler, J., 2019. The influence of water on the strength of olivine dislocation slip systems. *J. Geophys. Res. Solid Earth* 124, 6542–6559.
- Tilhac, R., Ceuleneer, G., Griffin, W.L., O'Reilly, S.Y., Pearson, N.J., Benoit, M., Henry, H., Girardeau, J., Grégoire, M., 2016. Primitive arc magmatism and delamination: petrology and geochemistry of pyroxenites from the Cabo Ortegal complex, Spain. *J. Petrol.* 57, 1921–1954.
- Tilhac, R., Grégoire, M., O'Reilly, S.Y., Griffin, W.L., Henry, H., Ceuleneer, G., 2017. Sources and timing of pyroxenite formation in the sub-arc mantle: Case study of the Cabo Ortegal complex, Spain. *Earth Planet. Sci. Lett.* 474, 490–502.
- Tilhac, R., Oliveira, B., Griffin, W.L., O'Reilly, S.Y., Schaefer, B.F., Alard, O., Ceuleneer, G., Afonso, J.C., Grégoire, M., 2020. Reworking of old continental lithosphere: unradiogenic Os and decoupled Hf–Nd isotopes in sub-arc mantle pyroxenites. *Lithos* 354–355, 105346.
- Tommasi, A., Vauchez, A., 2015. Heterogeneity and anisotropy in the lithospheric mantle. *Tectonophysics* 661, 11–37.
- Tommasi, A., Vauchez, A., Fernandes, L.A.D., Porcher, C.C., 1994. Magma assisted strain localization in an orogen-parallel transcurrent shear zone of southern Brazil. *Tectonics* 13, 421–437.
- Tommasi, A., Godard, M., Coromina, G., Dautria, J.M., Barszczus, H., 2004. Seismic anisotropy and compositionally induced velocity anomalies in the lithosphere above mantle plumes: a petrological and microstructural study of mantle xenoliths from French Polynesia. *Earth Planet. Sci. Lett.* 227, 539–556.
- Tommasi, A., Vauchez, A., Godard, M., Belley, F., 2006. Deformation and melt transport in a highly depleted peridotite massif from the Canadian Cordillera: Implications to seismic anisotropy above subduction zones. *Earth Planet. Sci. Lett.* 252, 245–259.
- Tommasi, A., Vauchez, A., Ionov, D.A., 2008. Deformation, static recrystallization, and reactive melt transport in shallow subcontinental mantle xenoliths (Tok Cenozoic volcanic field, SE Siberia). *Earth Planet. Sci. Lett.* 272, 65–77.
- Tommasi, A., Baptiste, V., Vauchez, A., Holtzman, B., 2016. Deformation, annealing, reactive melt percolation, and seismic anisotropy in the lithospheric mantle beneath the southeastern Ethiopian rift: Constraints from mantle xenoliths from Mega. *Tectonophysics* 682, 186–205.
- Tribuzio, R., Thirlwall, M.F., Vannucci, R., 2004. Origin of the gabbro-peridotite association from the Northern Apennine ophiolites (Italy). *J. Petrol.* 45, 1109–1124.
- Tribuzio, R., Garzetti, F., Corfu, F., Tiepolo, M., Renna, M.R., 2016. U–Pb zircon geochronology of the Ligurian ophiolites (Northern Apennine, Italy): Implications for continental breakup to slow seafloor spreading. *Tectonophysics* 666, 220–243.
- van Roermund, H.L.M., Boland, J.N., 1981. The dislocation substructures of naturally deformed omphacites. *Tectonophysics* 78, 403–418.
- Varas-Reus, M.I., Garrido, C.J., Marchesi, C., Bodinier, J.-L., Frets, E., Bosch, D., Tommasi, A., Hidas, K., Targuisti, K., 2016. Refertilization processes in the subcontinental lithospheric mantle: the record of the Beni Bousera orogenic peridotite (Rif Belt, Northern Morocco). *J. Petrol.* 57, 2251–2270.
- Varas-Reus, M.I., Garrido, C.J., Marchesi, C., Bosch, D., Hidas, K., 2018. Genesis of ultra-high pressure garnet pyroxenites in orogenic peridotites and its bearing on the compositional heterogeneity of the Earth's mantle. *Geochim. Cosmochim. Acta* 232, 303–328.
- von Raumer, J.F., Bussy, F., Schaltegger, U., Schulz, B., Stampfli, G.M., 2013. Pre-Mesozoic Alpine basements—their place in the European Paleozoic framework. *GSA Bull.* 125, 89–108.
- Wang, C., Liang, Y., Dygert, N., Xu, W., 2016. Formation of orthopyroxenite by reaction between peridotite and hydrous basaltic melt: an experimental study. *Contrib. Mineral. Petrol.* 171, 77.
- Wang, C., Lo Cascio, M., Liang, Y., Xu, W., 2020. An experimental study of peridotite dissolution in eclogite-derived melts: Implications for styles of melt–rock interaction in lithospheric mantle beneath the North China Craton. *Geochim. Cosmochim. Acta* 278, 157–176.
- Zhang, J., Green, H.W., Bozhilov, K.N., 2006. Rheology of omphacite at high temperature and pressure and significance of its lattice preferred orientations. *Earth Planet. Sci. Lett.* 246, 432–443.
- Zimmerman, M.E., Zhang, S.Q., Kohlstedt, D.L., Karato, S., 1999. Melt distribution in mantle rocks deformed in shear. *Geophys. Res. Lett.* 26, 1505–1508.